ABSTRACT

Title of Document: NANOPOROUS AAO: A PLATFORM FOR REGULAR HETEROGENEOUS NANOSTRUCTURES AND ENERGY STORAGE DEVICES

Israel Perez, Doctor of Philosophy, 2009

Directed By: Professor Gary W. Rubloff
Department of Materials Science and Engineering
and the Institute for Systems Research

Nanoporous anodic aluminum oxide (AAO) has vast implications as a tool for nanoscience research and as a nanostructure in which nanoscale devices can be fabricated because of its regular and ordered nanopores. Self-assembly plays a critical role in pore ordering, causing nanopores to grow parallel with one another in high density. The mild electrochemical conditions in which porous AAO grows along with its relatively cheap starting materials makes this nanomaterial a cost effective

alternative to advanced photolithography techniques for forming high surface area nanostructures over large areas.

In this research, atomic layer deposition (ALD) was used to deposit conformal films within in nanoporous AAO with hopes to 1) develop methodologies to characterize ALD depositions within its high aspect ratio nanopores and 2) to better understand how to use nanoporous AAO templates as a scaffold for energy devices, specifically Metal-Insulator-Metal (MIM) capacitors. Using the nanotube template synthesis method, ALD films were deposited onto nanoporous AAO, later removing the films deposited within the templates nanopores for characterization in TEM. This nanotube metrology characterization involves first obtaining images of full length ALD-AAO nanotubes, and then measuring wall thickness as a function of depth within the nanopore. MIM nanocapacitors were also constructed in vertical AAO nanopores by deposition of multilayer ALD films. MIM stacks were patterned into micro-scale capacitors for electrical characterization.

NANOPOROUS AAO: A PLATFORM FOR REGULAR HETEROGENEOUS NANOSTRUCTURES AND ENERGY STORAGE DEVICES

By

Israel Perez

Dissertation submitted to the Faculty of the Graduate School of the
University of Maryland, College Park, in partial fulfillment
of the requirements for the degree of
Doctor of Philosophy
2009

Advisory Committee:
Professor Gary W. Rubloff, Chair
Professor Sang Bok Lee
Professor Lourdes Salamanca-Riba
Professor John Cumings
Professor Luz Martinez-Miranda

Dedication

I would like to dedicate this dissertation to all the family, friends and educators who have helped me achieve this lofty goal. To my fellow students at the University of Maryland who have collaborated with me in this research including Parag Banerjee, Erin Robertson Cleveland, Laurent Henn-Lecordier, Nicholas Mostovych, Stefanie Sherrill, Ran Liu and Lauren Haspert, Also to the students whose helpful advice and discussion have helped me, including Susan Buckhout-White, Xiaolong Luo, Xia Bai. To the postdocs/research scientist who gave me great advice, including Dr. Sang Jun Son, and Dr. Sung-Kyoung Kim. To my advisors, Prof. Gary Rubloff and to my unofficial second advisor Prof. Sang Bok Lee, thank you for giving me the opportunity to contribute to your research.

I would also like to also dedicate this research to my immediate and extended family, specifically my mom, dad and two brothers. Also, to my grandmother who passed away during the writing of this dissertation at the age of 105. And last but not least to my wife, Colleen, who I could not live without.

Table of Contents

Chapter 1. Introduction

1.1. Porous Anodic Aluminum Oxide

To a significant extent, the promise of nanotechnology may well be realized in devices and nanostructures that employ (1) *pattern definition* through nanofabrication (typically, increasingly challenging lithography), (2) *self-alignment* in which conventional processes of material addition or subtraction can be used to form more complex 3D structures, and (3) nature's tendency toward *self-assembly*. Both pattern definition and self-alignment are already hallmarks of the most advanced micro- and nano-scale technologies today, such as in complex semiconductor devices and circuits, where the watchword is to maximize self-alignment in relation to tiny patterns formed by difficult lithographic steps whose number should be minimized.[2-4] Substantial attention and effort in nanoscale science and technology is aimed at exploiting self-assembly, a pathway with potential to reduce complexity and cost of pattern definition.

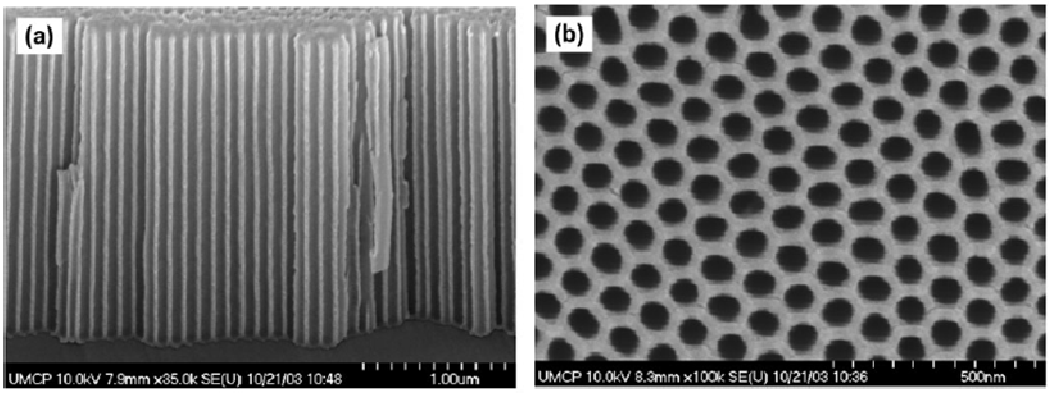

Figure 1.1 Porous AAO formed in 0.3M oxalic acid at 40V, a) side view, b) top view showing hexagonal ordering of pores.[11]

Porous anodic aluminum oxide (AAO) is an example of a material whose nanostructure is defined by self-assembly. It has become an important material because its nanopores naturally self-assemble and self-order creating a highly dense, straight-pore membrane over large areas by a simple electrochemical process. Porous AAO is one of the cost effective pathways to study nanoscale phenomena as evidence of its many uses including, nanowire growth [5, 6], catalytic membranes [7], templated nanomaterials [8, 9], and nanostructured devices [10]. This materials cost-effectiveness stems from the mild electrochemical conditions in which it can grow in an ordered manner over large areas and from the relatively cheap starting material, aluminum, from which it is made.

Porous AAO had its beginnings in metal finishing science in which thick oxides were created on aluminum to protect the metal from corrosion. As opposed to

air-formed or barrier-type anodic oxide films on aluminum, porous AAO films followed by a pore-sealing processes were attractive because under similar anodic conditions, much thicker oxide films could be made reducing the access of corrosive environments to the metal.[12] In the mid 1990s, Masuda et al.[9] released the two-step anodization method, which took advantage of porous-AAOs tendency towards self-order under certain anodization conditions to create long range, well-ordered, and well-aligned porous membranes. Soon after, many groups took on the challenge of understanding these specific conditions which resulted in well ordered structures in porous AAO, creating processing techniques that allowed for large (on the order of mm) single domain ordered pore arrays[13] by imprinting an ordered texture onto the aluminum pre-anodization, and also finding fundamental links between the different self-ordering conditions.[14] Figure 1.1 shows a cross-section and topview of an porous AAO membrane.[11] At around the same time Martin et al.[8] was developing methods to utilize straight pore membranes, including both track-etched poly carbonate membranes and porous AAO membranes to create template-based nanotubes of a variety of different materials.

Applications of porous AAO can be separated into two groups: nanoparticle applications, *freed from templates*, and device applications, *built in templates*. Porous

AAO's introduction in the mid 90's centered around nanoparticles or nanomaterials released from the AAO template, including Masuda et al. [9, 15] who deposited metal into nanoporous templates later selectively dissolving the templates away with application in high surface area metal electrodes and for nanocomposites. Martin et al.[8, 16] developed a "template synthesis" route to mass producing nanotubes and nanowires. Using these techniques, other researchers have utilized template synthesis to create nanotubes for drug delivery[17-19], as biomarkers[20], and for single nanotube devices[21, 22].

Device applications of porous AAO utilize the structure as a scaffold to hold active materials, which benefit mainly from the high surface area and nanoscale aspects of the porous template. Some of the most important recent applications in this area are those involving energy conversion and storage. Martinson et al.[10, 23-25] have done extensive research on porous AAO as scaffold for dye-sensitized solar cells. Lee et al.[26, 27] utilized MnO2/Poly(3,4-ethylenedioxythiophene) coaxial nanowires embedded in porous AAO taking advantage of the short diffusion paths afforded by the nanoscale pores for creation of an electrochemical supercapacitor. In-template porous-AAO energy and storage devices benefit not only from phenomenon like the short diffusion length in these nanowires but also by the surface area enhancement of

these porous templates.

In this research, porous AAO is studied as a nanostructure in which energy devices can be built, benefiting from high surface area inherent to this structure. In order to build devices within porous AAO, we must first understand the deposition characteristics of materials deposited into the template. I present here a nanotube metrology method for which deposition characteristics can be examined for films deposited into the high aspect ratio pores of AAO. This methodology helps shed light on the limitations of deposition into high aspect ratio nanostructures, and the proper adjustments needed to coat the porous AAO template uniformly. Also, an electrostatic metal-insulator-metal (MIM) device built inside porous AAO templates is presented. This device is achieved by the sequential deposition of thin-films onto porous AAO substrates using atomic layer deposition (ALD).

1.2. Nanotube metrology

Different deposition techniques applied to porous AAO membranes, including surface sol-gel,[21, 28] electro-deposition,[29] electroless deposition,[30] and gas phase deposition[31] have yielded nanotubes and nano-rods with uniform sizes and dimensions through the template-based synthesis technique. Chemical Vapor Deposition (CVD) is a commonly used gas phase deposition technique in which two

gas phase precursors are dosed into a reaction vessel under conditions leading them to react on the surface of a substrate to create a desired material. One example of CVD deposition into nanoporous AAO is seen for the deposition of boron nitride into porous AAO templates of 0.2μm nominal pore diameter.[32] In general, CVD step coverage into high-aspect ratio nanostructures such as Dynamic Random Access Memory (DRAM) trenches or nanoporous substrates is limited due to diffusion of precursors uniformly down to the bottom of the pores or trenches. Atomic Layer Deposition (ALD) is a technique derived from CVD, which sequentially doses reactant precursors separately, so that surface reactions are self-limiting.[33] ALD can achieve full step coverage in even the most challenging of nanostructured substrates due to the self-limiting nature of its deposition reactions.

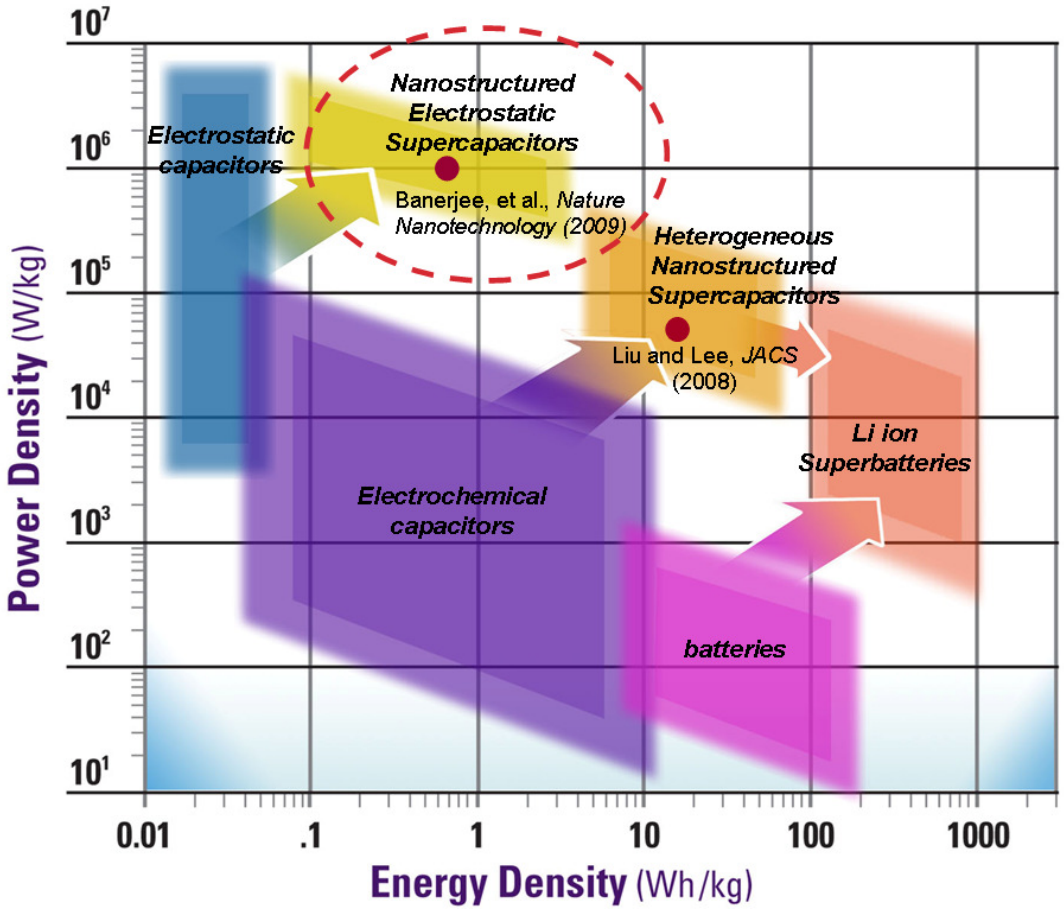

Figure 1.2 Ragone plot detailing the state-of-the-art in energy storage technologies comparing them as power density as a function of energy density

In this research, we have fabricated nanotubes using atomic layer deposition (ALD) into nanopore arrays created by anodic aluminum oxidation (AAO), developed and applied a TEM methodology to quantify the ALD conformality in the nanopores (thickness as a function of depth), and compared results to existing models for ALD conformality. ALD HfO_2 nanotubes formed in AAO templates were released by dissolution of the anodic alumina, transferred to a grid and imaged in TEM. An algorithm was devised to automate the quantification of nanotube wall thickness as a

function of position along the central axis of the nanotube, using a cylindrical model for the nanotube. Diffusion limited depletion occurs in the lower portion of the nanotubes and is characterized by a linear slope of decreasing thickness. Experimentally recorded slopes match well with two simple models of ALD within nanopores put forth in the literature. The TEM analysis technique provides a method for rapid analysis of such nanostructures in general and also a means to efficiently quantify ALD profiles in nanostructures for a variety of nanodevice applications.

1.3. AAO based electrostatic capacitors

Energy storage is an important area that can benefit from breakthroughs in nanoscience. Figure 1.2 shows a Ragone plot that details the state-of-the-art in energy storage technologies in terms of power density and energy density. Ideal energy storage technologies would have high energy density (capacity to store charge) and at the same time would boast high power density, (rapid charge and discharge rates). Current battery technology has very good energy density but lacks power density because of its dependence on bulk ionic movement and/or chemical reactions to charge and discharge. Recent, breakthroughs in lithium ion superbatteries show that coupling nanostructure and the materials science of the bulk material can lead to a higher power density.[34] Electrochemical capacitors store charge in the form of an ionic double

layer close to the surface of an electrode, so energy density depends on the surface area of the electrodes. Nanostructured surfaces utilized in the construction of electrochemical capacitors can provide high surface area, increasing energy density capabilities, while still providing high power density intrinsic to this technology as seen in recent literature.[26] Likewise, electrostatic capacitors energy density capabilities are dependent on electrode surface area, and can also benefit from surface enhancements provided by nanostructured materials. Electrostatic capacitors store charge in a thin dielectric material separating to metal electrodes, and are not limited by electrochemical reactions or ionic conduction to release or carry charge. Electrostatic capacitors lack energy density when compared to electrochemical devices, but are not limited in terms of charge-discharge rates making them perfect for burst-applications.

In this research, electrostatic nanocapacitors are formed by applying multi-layer metal-insulator-metal (MIM) thin films, deposited by ALD onto AAO substrates. The capacitance of this structure is studied depending on the depth and diameter of the pores grown using the AAO process. Metallic materials used for this structure include titanium nitride (TiN) and aluminum doped zinc oxide (AZO), while dielectric insulators studied were aluminum oxide (Al_2O_3) and hafnium oxide (HfO_2). Other electrical characteristics of these MIM capacitors are studied and discussed including

leakage current and dielectric breakdown.

Chapter 2. Anodic Aluminum Oxide

This chapter gives background on the anodization of aluminum, focusing on the concepts that are most critical to the deposition of materials into these templates, and the eventual design of electrostatic MIM capacitors within them. I detail some of my contributions in streamlining the AAO procedure, including development of computer controlled anodization software and design of anodization holders for both small experimental aluminum samples and also 2in wafer samples. Finally anodic bonding technique, in which ultra pure aluminum foil is bonded to glass, is detailed here. This technique allows for the two-step anodization procedure to be carried out on 2in wafers, protecting the usually flimsy aluminum foil from bending during subsequent processing steps during device fabrication.

2.1. Background and Motivation: AAO

The anodization of aluminum is an electrochemical process in which an alumina layer can be formed on an aluminum substrate in an electrolytic forming solution. Forming solutions contain reactive anions that oxidize the aluminum and also, in the case of acidic or basic solutions, etch the oxide formed. Depending on the nature of the solution (acidic, neutral, basic) oxidation will occur by different film growth mechanisms. Anodization at neutral pH in an electrolytic solution in most cases will

create a nonporous Barrier Anodic Alumina (BAA) film. At room temperature in an oxygen environment, aluminum has a 2-3nm native/barrier oxide film. When aluminum is anodized at constant potential in a neutral pH solution, i.e. phosphate solution, the native barrier oxide film is thickened at a constant rate of 1.2 nm V^{-1}[35]. In slightly acidic or basic solutions (or for long time periods in neutral solutions [36]), the anodization of aluminum leads to the formation of a Porous Anodic Alumina (PAA) film. In their review article, Thompson and Wood[12] described the formation of PAA as a balance between field-assisted/chemical dissolution at the electrolyte/oxide interface and oxide formation at the oxide/metal interface. Field-assisted dissolution at the pore base is caused by the stretching of Al-O bonds under high field, leading to the dissolution of Al^{3+}, a process aided by Joule heating caused by the high field at the pore tips[12]. It is misleading to describe anodic films grown on aluminum as aluminum oxide films because depending on the forming acid, much of the film can be composed of acid anion species incorporated in alumina. In their review article , Thompson and Wood[12] described anodic films formed on aluminum as containing two layers: “relatively pure alumina” and “anodic film material.” During anodization, the “relatively pure alumina” region sits directly on top of the metal surface while the “anodic film material,” which is composed largely of incorporated species other than

alumina, sits in-between the forming solution and the pure alumina region. For anodization in oxalic acid, the pure alumina region only extends out from the aluminum substrate for 13% of the total barrier layer thickness, which means the majority of the anodic alumina on the outer surface of the template is filled with anion impurities.[37]

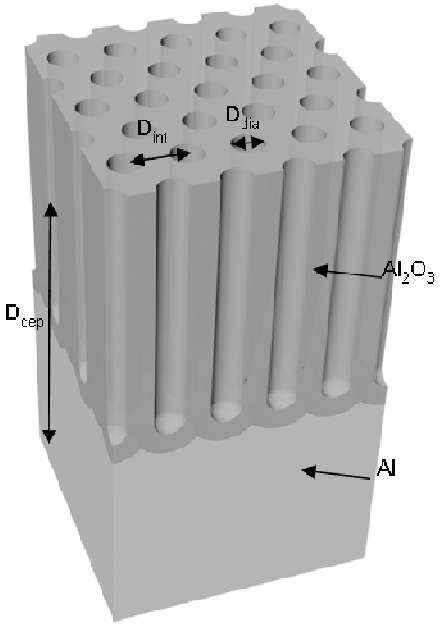

Figure 2.1: 3D schematic of PAA with labeled metrics.

Another interesting property of PAA is the hexagonal self-ordering seen in specific anodization conditions. Three types of weakly acidic solutions are known to lead to optimum self-ordering PAA: 2.7wt% aqueous oxalic acid at 40V, 20wt% aqueous sulfuric acid at 19V and 10wt% phosphoric acid at 160V[38]. Figure 1.1(a-b)[11] shows SEM images of a PAA template anodized in 0.3M oxalic acid (aqueous) at 40V and 8°C. As visible from the top down image (Figure 1.1b), pores order in a hexagonal arrangement with respect to each other. Sulfuric, oxalic and phosphoric acid solutions lead to hexagonally ordered pore arrays, but with different

interpore spacings, D_{int}, and pore diameters, D_{dia} (see Figure 2.1). In general the interpore spacings and pore diameters of PAA are linearly proportional to the anodizing potential. Pore diameters have a proportionality constant λ_p which it approximately 1.29 nm V^{-1}[39, 40]:

$$D_p = \lambda_p \cdot U \tag{2.1}$$

where D_p is the pore diameter in nanometers and U is the potential in volts. Interpore spacings have a proportionality constant λ_c which is approximately 2.5 nm V^{-1}[14, 39], which is roughly twice the rate of BAA thickening rate mentioned above:

$$D_c = \lambda_c \cdot U \tag{2.2}$$

where D_c is the interpore spacing in nanometers and U is the potential in volts. Experimentally, interpore spacings for sulfuric (U~25V), oxalic (U~40V) and phosphoric (U~200V) solutions are 66.3nm, 105nm, and 501nm, respectively, while their pore diameters are 24nm, 31nm, and 158nm, respectively. [14] Interestingly enough, for each of these forming acids, the porosity of the film is always ~10% and the maximum domain size (2D "grains" of pores ordered hexagonally) is 1-3μm[14, 38].

The self-ordering nature of PAA allows for the fabrication of highly ordered, large area nanoporous structures without the use expensive photolithography techniques. To

take advantage of the self-ordering in these structures, a two step anodization procedure is utilized[41]. An aluminum layer is first anodized for 10-20hrs (depends on acid type since, each acid has a different growth rate for sulfuric > oxalic > phosphoric[12]) to reach optimum ordering[14, 41]. The 1st anodization is then removed in a mixture of phosphoric acid (6 wt%) and chromic acid (1.8%) at 60°C. This leaves the underlying aluminum layers surface pre-textured with dimples ordered hexagonally by the pore bottoms. During the 2nd anodization, pores nucleate over each of the dimples in the surface, leaving an ordered PAA array. Pore depths (D_{dep}, Figure 2c) can be controlled by 2nd anodization time, and pore diameters (D_{dia}) can be controlled by a pore widening technique typically done in 0.1M phosphoric acid solution at 38°C.

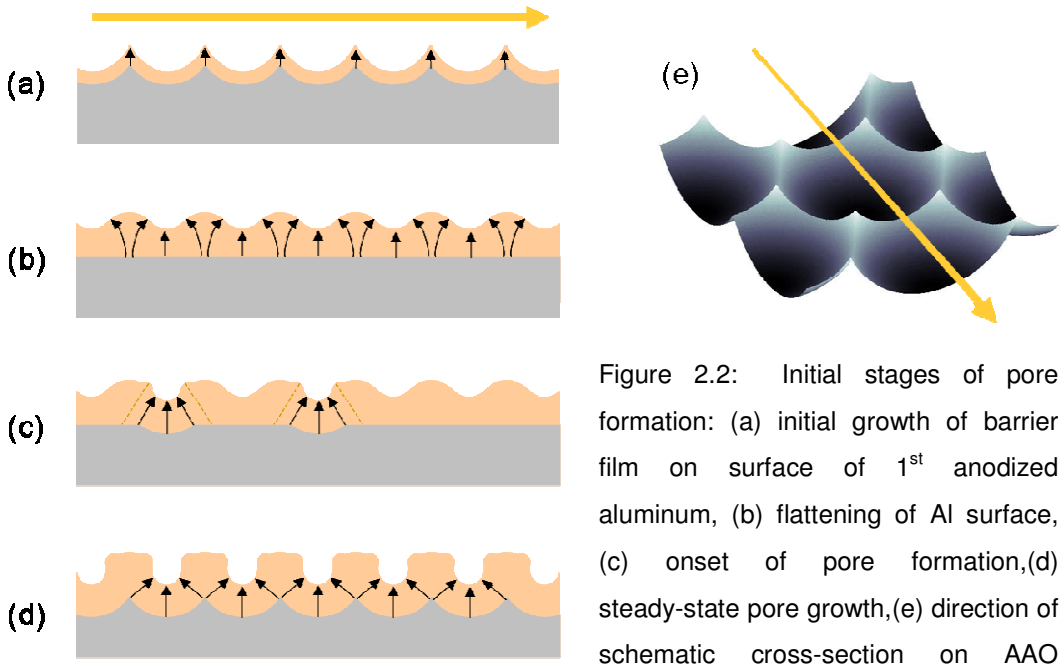

Figure 2.2: Initial stages of pore formation: (a) initial growth of barrier film on surface of 1st anodized aluminum, (b) flattening of Al surface, (c) onset of pore formation,(d) steady-state pore growth,(e) direction of schematic cross-section on AAO surface

The pore initiation stages at the beginning of an anodization determine the final top surface structure of the porous AAO template. Figure 2.2 is a schematic diagram of the initial pore formation stages on a 1st anodized surface. At the onset of anodization, a barrier AAO film is quickly formed (Figure 2.2 a-b) and the surface texture that developed on the aluminum during the long 1st anodization is flattened. Flattening of these surface peaks is due to the higher electric field during anodization which directly influences the oxidation rate, flattening the aluminum and forming protrusions in the anodic alumina. After barrier thickness is maximized for the applied potential (see equation 2.1), the electric field across the barrier film is highest for the areas over the middle of the divots which are thinner. Researchers also have

evidence that cracking and healing events due to stress in the film occur further thickening the area around the thin regions in the film (see Figure 2.2c dotted lines)[42]. The electric filed concentration starts the dissolution of the anodic alumina through a phenomenon discussed above termed field-assisted dissolution. As the anodic film is dissolved above the thinner regions, oxidation proceeds at the metal oxide interface to offset the further thinning of the anodic film. The balance of the dissolution at the electrolyte/oxide interface, and the oxidation at the metal/oxide interface under certain anodization conditions discussed above is termed steady state growth in which pores can continually grow as long as conditions at the pore tips stay the same(see Figure 2.2d). An outcome during these initial stages of anodization significant to our MIM devices described in chapter 4 to is that the surface texture (the sharp peaks) is transferred to the top surface of the final porous AAO template. These surface peaks are discussed in more detail in chapter 4 with respect to their influence on electrical properties of MIM capacitors built on porous AAO substrates.

2.2. Materials and Methods

2.2.1. Materials

Aluminum foil, 0.25mm (0.01in) thick, annealed, 99.99% (metals basis) aluminum foil was purchased from Alfa Aesar Corp. (Item #40761). Aluminum of different thicknesses were used when necessary (i.e. thickness ~ 0.5mm to increase rigidity of substrate during subsequent processing steps, thickness ~0.1mm for anodic bonding of foil to glass substrates), but always of 99.99% (metals basis) or better for anodization. perchloric acid, 70%, reagent grade from Fisher Scientific, was used to make solution for electropolishing. Oxalic Acid (solid), dihydrate 99+%, extra pure, from Acros Organics, was used to make solution for anodization of porous AAO membranes. All other chemicals used for wet etching procedures, including chromic acid, phosphoric acid, sodium hydroxide and ammonium hydroxide were of certified or reagent grade.

2.2.2. Two-step anodization procedure

The two-step anodization procedure was first reported by Masuda et al.[41]. Aluminum foil of high purity, 99.99% (metal basis) or better, was used for this anodization procedure. As received aluminum was first electropolished to remove

micro-roughness from the surface, which can greatly influence quality of the final pores. The as received aluminum was placed into a 1:5 perchloric acid in ethanol bath that was continually cooled down to ~3°C. A jacketed beaker was used to hold the bath, while a circulator pumped a 1:1 mixture of ethylene glycol and water through the jacketed portion of the beaker to keep the bath cool during electropolishing. Stirring was also very important to keep the solution at a low temperature and also to keep the perchloric acid concentration even throughout solution. This is an anodization procedure so, the aluminum sample was the positive electrode (anode) and stainless steel or aluminum piece of greater area was put into the solution as the negative electrode (cathode). Electropolishing was done for 5 minutes, or until aluminum surface was mirror like. Temperature was critical to achieving a mirror-like finish, which could not be achieved for starting solution temperatures higher then 5°C.

Anodization of aluminum proceeded as follow: Electropolished aluminum pieces were anodized at 40 V and 8°C in an electrolytic bath of oxalic acid (0.3M in deionized water). The circulator and bath setup was identical to the above setup for electropolishing. Typical 1st anodization time is ~7 hrs, allowing the AAO pores to reach an optimum ordering. Removal of the anodic oxide formed in the 1st anodization was done by etching in an aqueous mixture of phosphoric acid (6 wt %)

and chromic acid (1.8 wt %) at 60°C with light stirring, leaving a pre-textured and ordered aluminum surface. A second anodization of the aluminum under the same conditions of the first anodization leads to well ordered, and straight nanopores that are parallel to each other and perpendicular to the substrate. The pore depth is tailored by timing the 2nd anodization noting that the pore growth rate ~73nm/min. The 1st anodization was done using large pieces of aluminum, while the second anodizations were done by cutting smaller pieces off the bulk 1st anodizing sample and anodizing them using a sample holder. This sample holder exposed only a circular area in the middle of a 16x16mm square sample, where AAO was grown, and kept the samples at equal distance from the cathode from run to run (see appendix *i.b* for more on sample holder). After a template of desired pore depth is anodized, pore widening can be done in 0.1M (aq.) phosphoric acid solution at 38°C. The etch rate of the AAO under these conditions is ~0.79 nm/min. The initial pore diameter is ~35nm and the maximum pore diameter is ~90nm, and is limited by the interpore spacing of the AAO (~105nm). (*appendix i.a for more on pore widening*)

2.2.3. Anodic bonding of Al foil to glass wafers

In certain instances, larger sample sizes were needed for processing of devices on

AAO. Since, aluminum foil is a very flimsy substrate material, it is very difficult to go through the photolithography processes without bending/damaging the AAO sample. Initially, instead of using aluminum foil as a substrate, 2in Si wafers were used with sputtered aluminum. Sputtered aluminum has a limitation on film thickness, which is typically ~10μm after which films will be very uneven, and could have problems with film stress and delamination. Since, at minimum the 1st anodization time is ~7hrs, 10 μm of sputtered aluminum is not enough to complete both a 1st anodization which would optimizes order and a 2nd anodization which grows the usable template (growth rate of aluminum is 73nm/min).

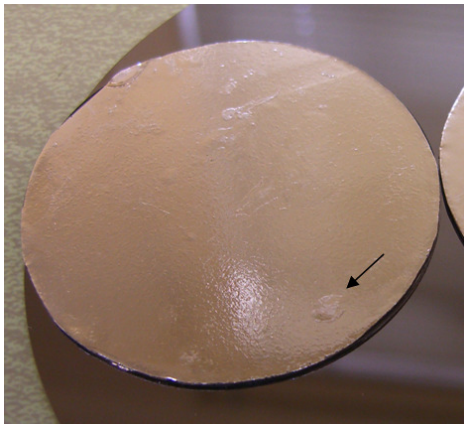

Figure 2.3:, Anodically bonded aluminum foil to a 2in glass wafer. Arrow denotes air bubbled form during process.

In order fabricate on substrate devices with optimum ordering, an anodic bonding technique was developed to attach the standard aluminum foil to 2in glass wafers. Anodic bonding was chosen over bonding with an epoxy since samples had be put in high temperature conditions during ALD deposition. High-purity, electropolished aluminum foils (99.99% Alfa Aesar) 200

mm thick were anodically bonded to 2-in glass substrates[76] at 380°C using a constant current of 0.7 mA. Figure 2.3 shows one of these substrates. One unresolved issue with this technique is that it was not possible to completely remove air pockets that formed at the bonding interface (see arrow in Figure 2.3).

Chapter 3. Nanotube Metrology

This chapter details the fabrication of HfO_2 nanotubes using atomic layer deposition (ALD) into nanopore arrays of porous AAO. My contributions involve the development and application of a TEM methodology to quantify the ALD conformality in the nanopores (thickness as a function of depth), and its comparison to existing models for ALD conformality. ALD HfO_2 nanotubes formed in porous AAO templates were released by dissolution of the anodic alumina, transferred to a grid and imaged in TEM. An algorithm was devised to automate the quantification of nanotube wall thickness as a function of position along the central axis of the nanotube, using a cylindrical model for the nanotube. Diffusion limited depletion occurs in the lower portion of the nanotubes and is characterized by a linear slope of decreasing thickness. Experimentally recorded slopes match well with two ALD models for deposition within nanopores put forth in the literature. This TEM analysis technique provides a method for rapid analysis of nanostructures and also is a means to efficiently quantify ALD profiles in nanostructures for a variety of nanodevice applications.

3.1. Background and Motivation: Nanotube Metrology

One intriguing example is the combination of nanopore self-assembly in anodic aluminum oxide (AAO) formation together with electrochemical deposition (ECD) of

materials into the AAO pores in a self-aligned manner to form nanotube or nanowire structures. Using appropriate polymeric materials in nanopore arrays, fast electrochromic displays have been demonstrated, where the short distances required for ion diffusion in the nanostructures enables higher frames per second (fps) rates compatible with video display technology.[27, 43] Researchers have also used atomic layer deposition (ALD) as an alternate self-aligned process to form nanotubes or nanowires in AAO,[31, 44, 45] taking advantage of ALD's unprecedented capability for thickness control (at the atomic scale) and conformality in the most demanding circumstances (aspect ratios of order 100X or more, i.e. depth/width). Atomic layer deposition (ALD) is a gas phase deposition technique which utilizes self-limiting chemistry to control film thicknesses down to the atomic scale. ALD employs alternating reactant exposures of two precursors which react on the surface sequentially to build thin films atomic layer by atomic layer. ALD proves to be an effective technique for the deposition of conformal films into high aspect ratio nanopores. However, conformality along the entire length of the pore is still a challenge in ALD due to diffusion limitations, although this problem can be alleviated in part by increasing exposure times during deposition runs.[7, 31, 44, 46]

While the perfection required in such ALD nanostructures depends on the

application, measuring geometrical profiles and tolerances will be crucial to most if not all applications. For example, wall thickness profiles of ALD nanotubes may well determine breakdown voltages and leakage current in energy capture or storage devices, while also determining efficacy of nanoparticle drug delivery systems built from such nanotubes. Metrology of 3-D nanostructures will therefore be crucial to a variety of device applications as well as to optimizing ALD processes. This is, however, a difficult challenge.

We report here an approach for efficient metrology of high aspect ratio nanotubes and its application to nanodevice structures employing ALD. It capitalizes on AAO templates for ALD nanotube fabrication, template dissolution and subsequent TEM imaging of the nanotubes, and algorithms for rapidly determining wall thickness profiles along the nanotube axis. For HfO_2 ALD nanotubes formed in AAO templates, we find that the resulting thickness profiles are in agreement with two prior models for ALD conformality. The approach demonstrated here presents a useful means for analysis of ALD process performance in nanostructure applications, as well as a more general method for metrology in some classes of relatively symmetric nanostructures.

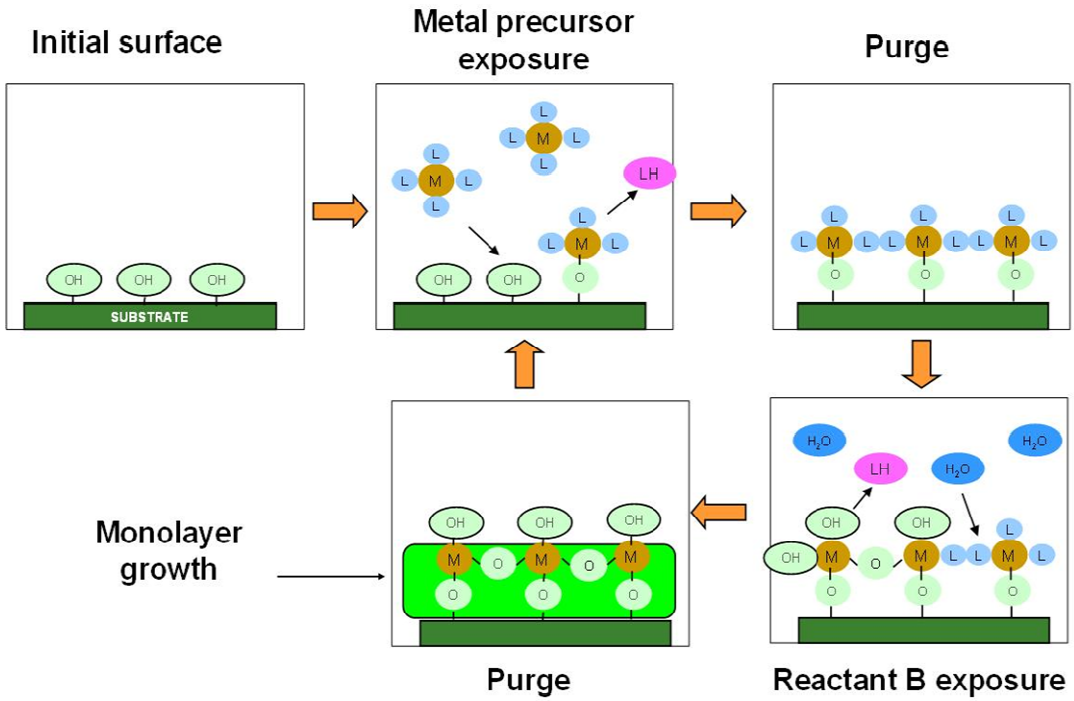

Figure 3.1 Schematic of one ALD cycle.

3.1.1. Atomic Layer Deposition

Figure 3.1 is a schematic detailing the process flow of one ALD cycle. The initial substrate is first exposed to reactant A, a metal precursor which contains ligands that are susceptible to reaction with hydroxyl groups on the substrate. Once the surface is fully saturated with the metal precursor, excess precursor and reaction byproducts are purged from the reactor by an inert carrier gas (i.e. N_2, Ar…). Once the reactor is purged, reactant B, an oxidizer (i.e. H_2O, O_3,…) is dosed into the chamber, and reacts with remaining ligands unreacted during exposure A. Once the excess

precursor and reaction byproducts are purged out of the reactor, one ALD cycle is complete. Since each cycle deposits a discrete amount of material (as small as .05nm/cycle for some ALD chemistries), thin films can be deposited with film thickness resolution an the atomic scale.

3.1.2. Nanopore Metrology

Traditional techniques that attempt to experimentally measure thin films deposited in nanopores or trenches employ SEM or TEM which require lengthy sample preparation that typically involve sample cross-sectioning. Nanopores are especially difficult to cross section due to their one dimensional shape and small diameter. Ideally, the cross-sectional cut for a nanopore should be along the center axis of the nanotube in order to get an accurate measurement of sidewall film thickness along its full length. If the cut is not aligned with the pore axis wall thickness data can be skewed as a result of the pores' cylindrical character. If the cross-sectional cut is off center, film thickness measurements will be larger than actual film thickness. In most of the literature, nanopores are imaged by cutting a bulk nanoporous film parallel to the nanopores' axis and then searching along the cross section face to find pores that have been cut along their specific axis. Gordon et al. imaged a thin film deposited in

elliptical pores deep etched into silicon by cleaving the silicon along a natural crystallographic axis and imaging using a dual-beam SEM-FIB system which allows for further in situ cutting of the sample.[46] Elam et al. imaged a thin film deposited nanoporous anodic aluminum oxide (AAO) by embedding the film in epoxy and polishing perpendicular to the nanopore axis. This allowed for accurate measurement of film thickness within the pores at different depths in SEM. However, in order to obtain a highly resolved thickness profile for the full length of a pore it would require many iterations of polishing and SEM imaging for a single sample.[44] Employing traditional SEM cross-sectioning techniques to the characterization of films deposited along the full length of nanopores is possible, but proves to be time consuming and depends on the researcher's ability to apply cross-sectional cuts accurately along high aspect ratio structures.

3.1.3. ALD conformality - modeling and experiment

There have been several studies in the literature which attempt experimentally and/or theoretically to understand the ALD film deposition characteristics in nanopores or trenches.[44, 46-49] Gordon et al.[46] developed a simple theory that could generate

conditions for which full step-coverage could be attained within narrow high aspect ratio holes. This simple theory depends on the exposure time and partial pressure for the precursor species which limits conformality (deep penetration into the nanopore) in the ALD process. The theory predicts the expected partial pressure P and dose time t required to achieve full step-coverage in a pore for a given aspect ratio. Assuming a cylindrical pore with one open end, the equation is,

$$(Pt)_{total} = S\sqrt{2\pi mkT}\left[1+\frac{19}{4}a+\frac{3}{2}a^2\right] \tag{3.1}$$

where S is the saturation dose, m is the molecular mass, k is Boltzmann's constant, T is the temperature during exposure, and a is the aspect ratio of the nanopore. This equation applies to whichever precursor that limits conformality or penetration into the pores. Which reactant is the limiting precursor depends on the precursor's molecular mass (m), the size of the exposure dose (t) and also the partial pressure of the precursor during exposure (P). For example, from our experiments we can calculate the aspect ratio (a) depending on P, t, m and S for the separate precursors, water and tetrakis(ethylmethylamino)hafnium (TEMAH). For our experimental parameters (see section 5) we estimate the aspect ratio of a pore for which TEMAH can fully coat to be ~30 while the aspect ratio of a pore for which water can coat is ~90. So for our

experiments TEMAH is limiting the depth to which the ALD films can penetrate into the nanopores.

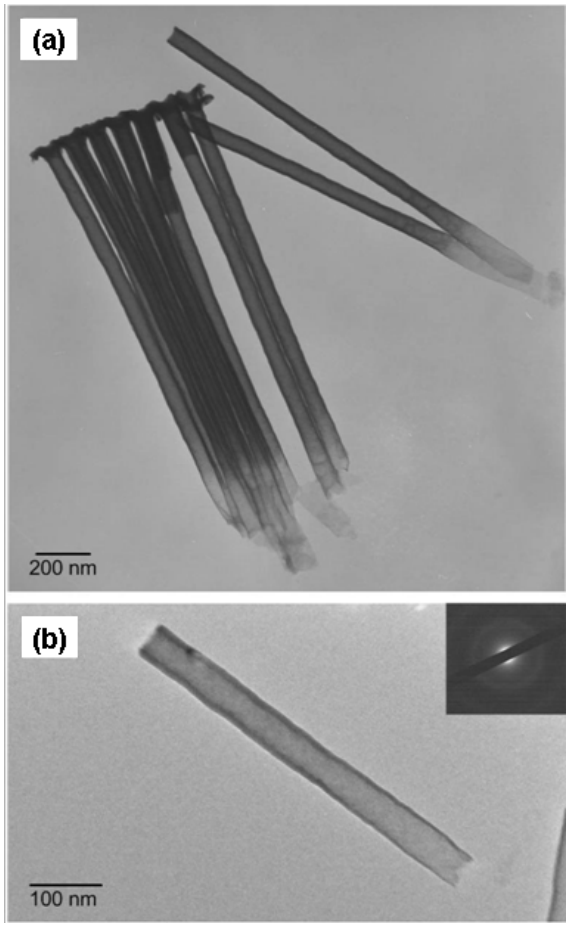

Figure 3.2: (a) TEM image of HfO2 nanotubes made by depositing HfO2 by ALD into AAO templates followed by template dissolution, (b) TEM image of single HfO2 nanotube with inset selected area diffraction pattern.[11]

Larger pressures and exposure times will allow the reactant to penetrate deeper in the nanopores while a larger molecular mass will hinder its ability to enter a nanopore. To fully coat the AAO nanopores in our experiments (4μm depth, 60nm diameter, aspect ratio ~70) the exposure time of TEMAH would have to be increased from 0.6 seconds to ~2 seconds.

Since the model deals with sub-micrometer diameters with gas pressures around 1 Torr, the mean free path of the molecules within the gas is much larger than the diameter of the pore. Therefore the assumption was made that gas diffusion within the pores could be

modeled by molecular flow in which there are no gas-phase collisions. Researchers backed this theory with experimental evidence by depositing HfO_2 by ALD into high aspect ratio holes etched in silicon. The holes for which the ALD precursor exposure times were higher than the value generated by the model exhibited full step-coverage, but those with lower than the value exhibited incomplete coverage, with thinning regions in the deeper portions of the pores.

Elam et al.[44] studied ALD deposition of Al_2O_3 and ZnO in the high aspect ratio pores of AAO membranes. The AAO membranes had pores with diameters of 65nm, depths spanning the full thickness of 50μm, and open ends on either side of the membrane. Plain view SEM images of the bottom, top and middle of the Al_2O_3 ALD deposited templates showed a dependence of film conformality on exposure time. Film thickness recorded from the middle of the template at some depth within a pore varied with exposure time when compared to thickness recorded near the top and bottom of the template. The ZnO ALD deposited AAO membranes showed similar results. Zinc compositional maps of cross-sectional profiles of the membranes created by an electron microprobe revealed smaller amounts of Zn near the center of the AAO cross-section for shorter exposure times. A simple Monte Carlo simulation was also submitted to explain variations with the step coverage due to insufficient exposure

times in both the Al_2O_3 and ZnO cases. The model assumed that molecular transport within the pores was governed by molecular flow and that the coatings reacted in a self limiting manner characteristic of ALD. The model sectioned a cylindrical pore into an adjustable amount sub-sections or elements. Each element can be reacted by a finite amount of precursor molecules depending on its surface saturation. Two random number generators were employed in the model, one governing the random walk of sets of reactants within the pores and the other governing the reaction of the sets to available un-reacted element of the pore. Once a set of reactants reacts with one of sectioned areas (elements), the cylindrical diameter of that section is decreased and the section is no longer available for further reaction during the current cycle. Since the length of each step in the reactants random walk decreases with decreasing local diameter, this modeling technique gives a dynamic picture of molecular flow and how it relates with ALD deposition of thin films within nanopores. In both Gordon's and Elam's studies experimental measurements of thickness trends along the depth of a nanotube were not extensively explored.

3.1.4. Our approach

Our approach was developed in order to measure thin films deposited in nanopores without extensive cross-sectioning. This was achieved via the use of anodic aluminum oxide (AAO) as a nanoporous template. One of the novelties of using AAO in this research is its ability to be removed by dissolution, releasing deposited materials into solution. This novelty is exploited in the template based synthesis method[8, 16, 31, 44, 50] to create nanotubes, nanorods and carbon nanotubes with very uniform structures and manufactured in high density. AAO films can be structured to comprise cylindrical nanopores with uniform dimensions (15-300nm diameters) distributed in a dense hexagonal array. Anodization conditions, including voltage, temperature and type of electrolytic solution, direct pores to self-assemble perpendicular to the substrate with control over pore depth and diameter.[9, 14, 38, 51, 52] Different deposition techniques applied to AAO membranes, including surface sol-gel,[21, 28] electro-deposition,[29] electroless deposition,[30] and gas phase deposition[31] have yielded nanotubes and nano-rods with uniform sizes and dimensions through the template-based synthesis technique.

In this paper, a simple and robust methodology is put forth detailing how to experimentally measure template-synthesized nanotubes processed by ALD. HfO_2

films were deposited, using ALD, to AAO templates which contained pores that were ~4 μm in depth and ~60 nm in diameter. TEM micrographs of single nanotubes from this sample were taken and analyzed using image analysis code based on a simple geometric model. Experimentally recorded trends for multiple nanotubes are presented as an example of this image analysis technique. These trends are then compared to results from recreated theoretical models outlined above and originally reported by Elam et al.[44] and Gordon et al.[46]

3.1.5. Cylindrical Assumption

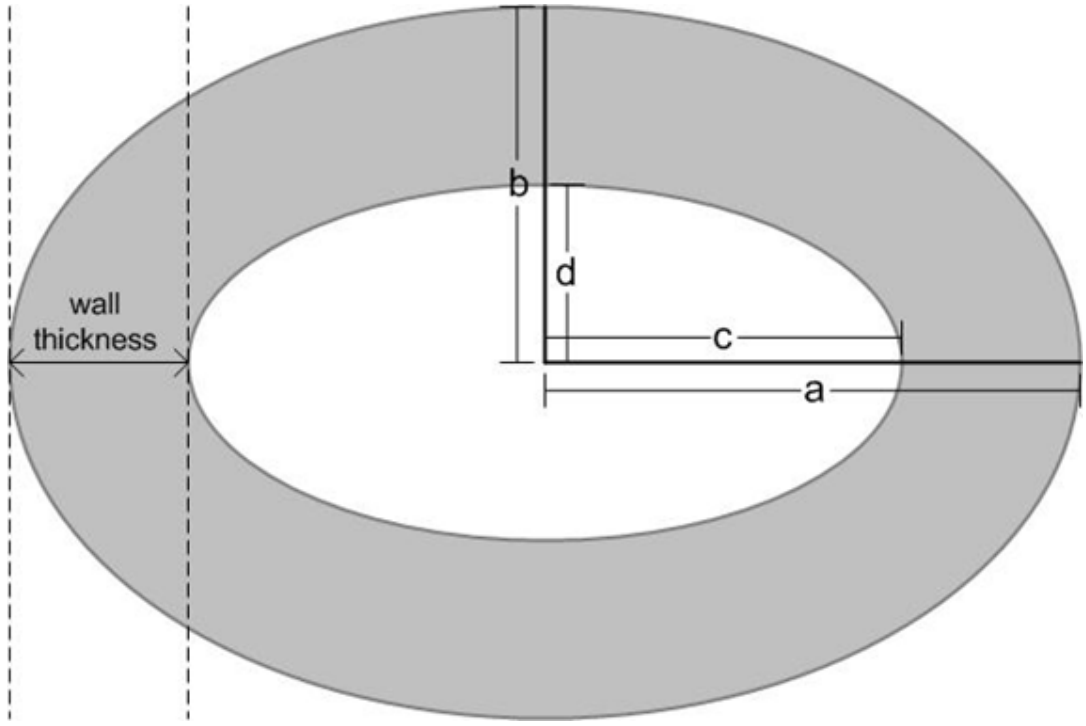

Figure 3.3: Cross-section of an elliptic cylinder.[11]

Nanotubes produced by the template synthesis method in AAO have a cylindrical shape, characteristic of the pores in which they are formed. This cylindrical shape can be seen in (a-b) . After ALD deposition to form nanotubes in the pores and subsequent dissolution of Figure 3.3a-b) appear in TEM as long rectangular ribbons with dark edges running along their lengths. The edges are attributed to the higher material density at the walls. At one end the nanotubes display a broadened structure reminiscent of the head of a nail, which is caused by the ALD HfO_2 material deposited on the top surface of the AAO between its nanopores. At the other end the nanotube walls thin due to the somewhat reduced deposition deeper into the AAO nanopore, indicative of deviation from perfect conformality (e.g., from depletion effects within the nanopore). Assuming that the nanotubes take on the shape of a cylinder, the thickness for which an electron would have to travel at any given point along cross-sectional line of length L perpendicular to the nanotube axis is:

$$L = 2\left[\sqrt{b^2\left(1-\frac{(x-a)^2}{a^2}\right)}-\sqrt{d^2\left(1-\frac{(x-a)^2}{c^2}\right)}\right] \tag{3.4}$$

where a is the horizontal outer radius, b is the vertical outer radius, c is the horizontal inner radius, and d is the vertical inner radius (see figure 3.3). This equation is plotted in Figure 3.4 for the case of an ideal cylinder and an elliptic cylinder. The two plots

are overlaid on cross-sections which are indicative of the nanotubes cylindrical nature. For the case of an ideal cylinder, parameter *a* should be equal to *b*, and parameter *c* should be equal to *d*. For the case of a film deposited in an elliptical shaped pore, the parameter equivalencies for an ideal cylinder would not hold true. However, as a result of the uniform deposition provided by ALD, the wall thickness of the elliptic cylinder created within this type of pore should be uniform, and therefore wall thickness would be equivalent to (a – c) which would be equivalent to (b – d). The parameter L can be correlated with image darkness associated with loss of TEM electron transmission through more material. In both cases in Figure 3.4, thickness profiles show that the thickest portion of each cylinder corresponds with the edge of the inner surface and the thinnest portion of the cylinder corresponds to its outer edge on either side of the cylinder.

3.1.6. Bright field TEM

Bright field TEM imaging records the intensity of electrons transmitted through a thin sample, so that darker areas indicate thicker or denser regions along the beam direction. As suggested by Figure 3.4, this permits nanotubes to be imaged as 2D projections along the beam axis. For polycrystalline samples, intensity differences in

bright field images are due not only to scattering losses associated with sample thickness but also to electron diffraction by the crystal lattice. Depending on how a crystal is oriented with respect to the beam, it will diffract more or less electrons, leading to a darker or brighter intensity in the image for the area of the crystal. In our experiments, the low temperature associated with the ALD process renders all HfO_2 films amorphous, so that crystal diffraction mechanisms do not contribute to the image. The amorphous character of the nanotubes was confirmed by selective area diffraction (SAD) patterns taken during the course of the TEM experiments (inset of Figure 3.2b). For amorphous and compositionally uniform samples, since the atoms in the material have no order, orientation of the sample with respect to the beam does not matter either. Thus the number of electrons passing through the sample will only be a function of the thickness of the deposited film. It is this property of the transmitted electrons in amorphous thin materials that is exploited for our analysis.

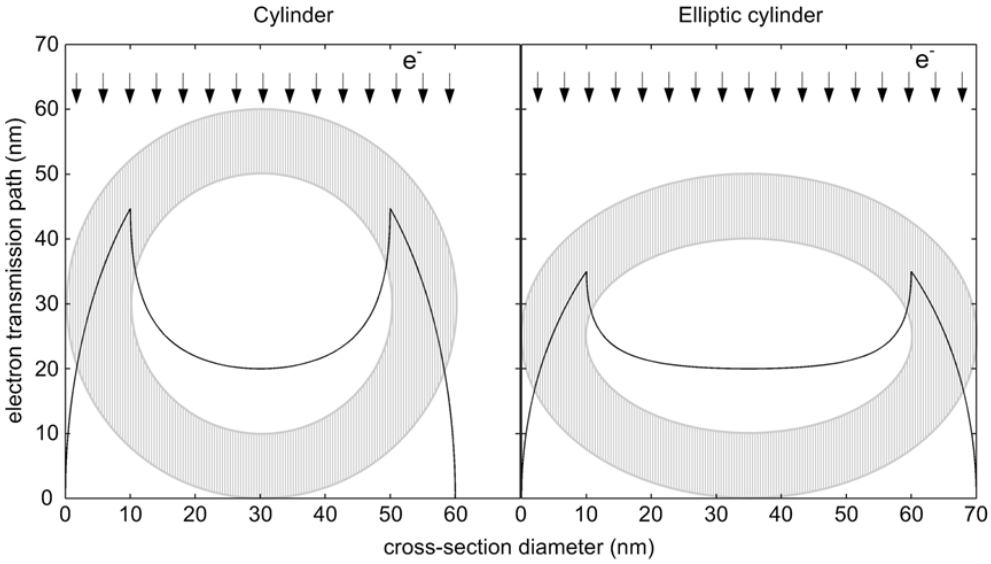

Figure 3.4: The electron transmission path through the nanotube with respect to the cross-sectional diameter of a cylinder. The cross-sectional intensity profile should mirror this thickness profile in a TEM micrograph since the main contribution to intensity variation is film thickness for amorphous materials.[11]

3.1.7. Image analysis

The simple geometric model outlined above can assist in the analysis of nanotubes imaged in bright field TEM. Application of this model to experimental intensity profiles can yield information about the dimensions of the nanotubes such as inner and outer diameter, and wall thickness. In Figure 3.5, an image of an amorphous HfO_2 nanotube is shown. An intensity profile was taken perpendicular to the central axis of the nanotube, with intensity data averaged over a 10nm portion along the nanotubes length. The plot in Figure 3.5 shows the data retrieved by the intensity profile. The data

consists of averaged (averaged along the 10nm length of the profile) 8-bit grayscale values with respect to the position along the profile. If we apply the cylindrical model to imaged nanotube we can denote the inner-diameter edge of the nanotube as the thickest part, and therefore the intensity values recorded in that area should be the lowest.

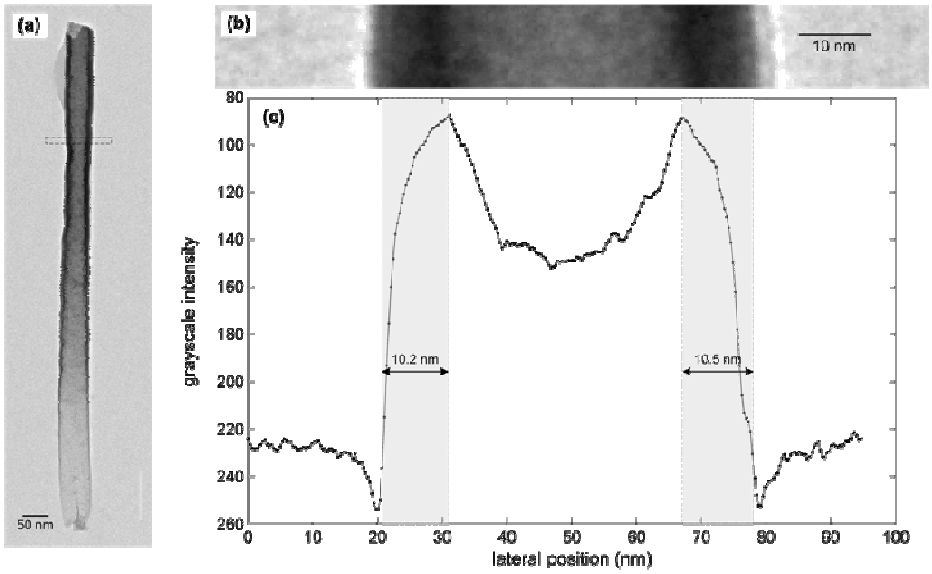

Figure 3.5 (a) TEM image of typical HfO2 nanotube, (b) Rectangular box from (a) which has been enlarged, (c) The intensity profile perpendicular to the center axis of a nanotube. The profile is averaged over a 10nm thickness. The plot shows the intensity variation as a function of the profile length. The distance between the minima in the data represents the inner diameter. The distance between where the data drops into the background is the outer diameter. Wall thickness can be measured for each side of the nanotube by measuring the distance from minima to background for both sides. The inlay in the image shows the selected area diffraction pattern of the nanotube. [11]

Likewise, the outer-diameter edge corresponds to the thinnest part in the profile,

and therefore the intensity values should be the highest or equivalent to the background of the image. Therefore the distance along the x-axis between where the data first meets the background and where the first minimum in the data occurs is equivalent to the wall thickness of one side of the nanotube. Similarly, the other sidewall thickness is equivalent to the distance between where the second minimum in the data occurs and where the data meets the background again. The wall thickness of the upper sidewall is 10.2 nm while the wall thickness of the lower sidewall is 10.5 nm for the example in Figure 3.5.

The line profile analysis method detailed above can be used to create a rapid characterization method for ALD conformality in high aspect ratio nanopores. Line profiles can be taken in succession along the whole length of a nanotube giving variation of outer diameter, inner diameter, and film thickness with respect to length from top to bottom. The outer diameter of the nanotube is defined by the AAO template in which it is formed. Thus for an AAO template with constant pore diameters along its whole depth, the nanotubes created should have constant pore diameters. In order to realize the rapid characterization method for ALD conformality a Matlab routine was developed. First, an image of a nanotube (similar to the image in Figure 3.5a) is inputted into the program and the user draws a multi-segmented line

through the center axis of the nanotube. The user also inputs various parameters such as the number of data points, data point separation, and area of the cut for which the wall thickness is measured. The Matlab routine will then take the user inputs and output a graph of thickness versus nanotube length.

All nanotubes measured by this method were isolated, broken-off pieces of a larger bulk nanotube film to avoid inaccuracies which might arise from nanotubes stacked closely together in an image. Even though we do not know exactly where each nanotube broke off from the bulk film, we can still estimate their aspect ratio using images which contain bunches of nanotubes intact from top to bottom (Figure 3.2a). These nanotubes have an approximate length of 1500nm and thickness about 60nm, i.e. an aspect ratio of 25X. This is consistent with the prediction (above) from Gordon's model that our experimental ALD process parameters should achieve conformality only to an aspect ratio of about 30X.

3.1.8. Beyond the cylindrical assumption

Experimentally we cannot assume that the nanotubes will always maintain a

cylindrical shape. Nanotubes with thin-film gradients along their lengths often look as if their outer diameters increase as their wall thicknesses thin. We believe this is an artifact of the drying process in which surface tensions cause thin walled nanotube portions to deform to an elliptical shape or flatten and collapse. The nanotubes inner and outer diameters are both equally affected by deformation in this manner during drying. During this deformation the inner and outer diameters of the nanotube should be equally affected. Depending on the thickness and properties of the film the collapse can be full or partial. A full collapse is characterized by the cylinder being completely flat with no access to its inner cavity. A partial collapse is characterized by the center part of the film collapsing but leaving cavities near the edges of the nanotube. In the case of a partial collapse, measurement methods should still hold true, since a quasi-cylindrical edge should still be available for measurement. Another artifact that could be of some importance is the differential strain built in by the process, particularly differential thermal expansion from cooling after ALD deposition. Since the thermal expansion coefficients in our case (substrate Al_2O_3 and film HfO_2) are similar, and our ALD process is done at a relatively low temperature (200°C) the change in dimension of the HfO_2 nanotubes due to stress relief upon release from the AAO template was estimated, using the standard relation

$$\varepsilon = (\alpha_2 - \alpha_1)\Delta T \tag{3.5}$$

This suggests only a tiny change in dimension (0.009%) due to the difference in thermal expansion coefficients of HfO_2 (1.31×10^{-6} C^{-1}) and Al_2O_3 (1.89×10^{-6} C^{-1}) that will occur upon cooling from the ALD growth temperature 200°C to room temperature.[53]

Variation of the inner diameter with depth into the AAO pore is governed by the ALD process. The number of cycles in ALD as well as the film thickness per cycle will define the inner diameter of the nanotube. Wall thickness measurements are simply made by subtracting the outer diameter from inner diameter and dividing by two. This measurement should be free from any artifacts caused by the collapse of the cylinder in thinner sections since as stated previously inner and outer diameters of the nanotube should be equally affected. Also, wall thickness measurements should not be affected by brightness of the electron beam when the image was taken or by any non-destructive post processing image adjustments (i.e. gamma, brightness, contrast,...). The minima in the data will always outline the inner diameter of the nanotube and the maxima in the data will always outline the outer diameter of the nanotube.

3.2. Materials and methods

3.2.1. AAO Procedure

A porous AAO template was synthesized by a two-step anodization method.[41]. In brief, a piece of electropolished aluminum foil (99.99%, Alfa Aesar) was anodized at 40V and 10°C in an electrolytic bath of 0.3M oxalic acid. In the first step of the anodization process, the foil was anodized for long enough (~ 7 hours) so that the pores were ordered and growing orthogonally with respect to the substrate. The AAO film that was created was then etched off by an aqueous mixture of phosphoric acid (6 wt %) and chromic acid (1.8 wt %), leaving a pre-textured and ordered aluminum surface. In the second step of the anodization process, the foil was anodized for a set amount of time (~1 hour) defining the depth of the pores to be ~4um. Pore diameters were adjusted to ~60 nm using a pore-widening solution of phosphoric acid (0.1 M) at 38 °C. Membranes were not detached from the substrate before ALD processing and therefore its nanopores only had one open end.

3.2.2. ALD Process

High-K dielectric HfO_2 thin films were deposited by alternating reactant exposures of tetrakis(ethylmethylamino)hafnium (TEMAH), that is, $Hf[N(CH_3)(C_2H_5)]_4$ [99.99%

grade, Sigma Aldrich], as the organometallic precursor and DI water as an oxidant. The ALD equipment consists of a stainless steel tube (25" in length and 3" in diameter) in a tube furnace. Precursors and nitrogen gases were introduced through one end of the reactor, while un-reacted precursors and reaction byproducts were exhausted at the opposite end of the tube to a rotary vane vacuum pump. Substrates were introduced into the system through a removable flange at the exhaust end of the reactor. The wafer temperature was measured via a thermocouple to be 200 ˚C.

During each of the self-limited half reactions corresponding to the alternating exposures of TEMAH and water, reactants were dosed to achieve full surface saturation resulting in excellent thickness control at the atomic level as a sub-monolayer of oxide was consistently deposited for each cycle.

A reservoir containing 5 g of liquid TEMAH was placed in an incubation oven set to 105 ˚C to achieve a vapor pressure of approximately 2 Torr. Prior to each exposure, the TEMAH gas was fed into a 20 mL isothermal volume and TEMAH doses were controlled by timing the opening of a pneumatically actuated valve. A 0.85 μmol dose of TEMAH was determined to be sufficient to achieve full saturation on a Si substrate located in next to the AAO template. In the case of water, the vessel was kept at room temperature. Accurate water dosage was achieved by filling up a 20 mL isothermal

volume up to a targeted pressure monitored by a capacitance gauge and then discharging the gas into the reactor for a fixed amount of time. This pressure end-point control approach was required to minimize the effect of the cooling of the water source over the process duration due to the forced vaporization of the precursor and the resulting decrease of its vapor pressure. Full saturation was achieved by filling up the volume at 7 Torr. We estimate the partial pressures of both the water and TEMAH doses to be ~7 mTorr from the pressure spike recorded by a downstream pressure sensor (average change in pressure over peak width).

Throughout the deposition process, 30 sccm of nitrogen was continuously flowed into the reactor maintaining a reactor pressure of 96 mTorr. A growth rate of 1 Å cycle^{-1} was achieved over 100 cycle process. Prior to each pulse, a 10 s N_2 purge was initiated to ensure that un-reacted precursor and reaction byproduct, mainly $(CH_3)(C_2H_5)NH$, were adequately purged out of the reactor.

3.2.3. TEM Characterization

After ALD deposition, samples were placed in 0.1M NaOH solution for 1 hour which dissolved away the alumina membrane freeing the HfO_2 film in solution. After filtration with DI water, a drop of the solution was placed on a carbon coated Cu TEM

grid. TEM studies were performed on a JEOL 2100 microscope with LaB_6 source operated at 200keV. Images of single nanotubes that had broken away from the bulk HfO_2 film and that were laying flat on the surface of the carbon film were taken with a post-column Gatan CCD camera. Images were then analyzed using the image analysis to be outlined below.

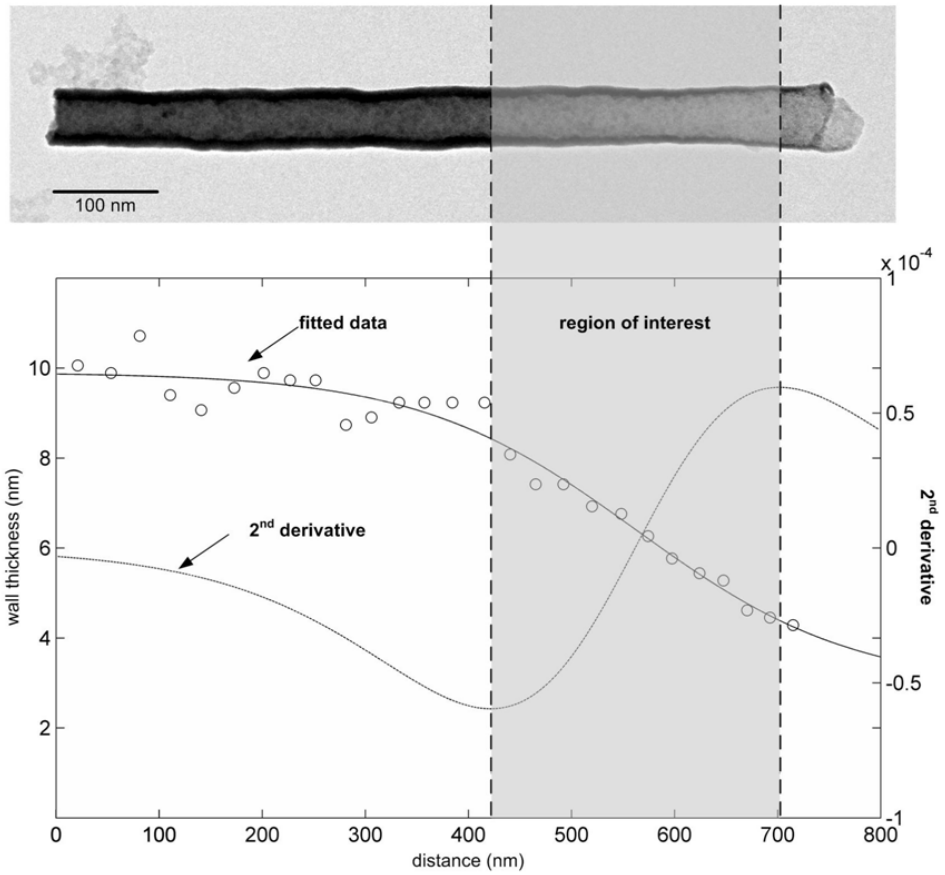

Figure 3.6 Schematic of how the data range was narrowed down to obtain a region of interest from which a linear slope could be extracted. The thickness data with respect to distance from the top to the bottom of the nanotube is fitted with a sigmoid curve. The 2nd derivative of the sigmoid curve is taken for which the maximum and minimum points define the region of interest.[11]

3.3. Results

3.3.1. Method of data extraction

Using the image analysis techniques discussed above, thickness profiles over the full measurable lengths of multiple individual nanotubes were made, yielding data of film thickness as a function of depth within AAO porous membranes. As explained above, not all nanotubes yielded from the templates were fully intact from top to bottom; e.g., isolated nanotubes as in Figure 3.2b were sometimes shorter than those that remained as bunches as in Figure 3.2a. Furthermore, one cannot rule out breakage/loss of the thinnest portion of the nanotubes. Nevertheless, thinning was readily observed near the deepest end of the examined nanotubes, and thus the rate at which the films thinned as a function of depth (or slope at the nanotube end) was fully measurable in this experiment. The thinning rate or slope is significant because it reflects the experimental parameters in ALD and the dimensions of the nanopores and can be compared to ALD conformality models. In Figure 3.6, thickness vs. length data is plotted for a single nanotube. This data was fit with a sigmoidal curve:

$$y = \frac{a}{1 + e^{-\frac{(x-a)}{c}}} + d \tag{3.6}$$

using the nonlinear least-squares regression method. This curve fit assisted with singling out a region of interest within the data by providing a smooth analytical curve through the data which helps to identify the region of decreasing thickness, i.e. the portion of the nanotube which is presumably most indicative of ALD depletion. The curve fit also facilitates more quantitative investigation: specifically, its 2^{nd} derivative with respect to position along the length of the nanotube provides a minimum and maximum at either end of the ALD depletion region (the region of prime interest), where curvature is highest in the original sigmoid fit. A linear regression was then fit to the extracted data in this ALD depletion region, and the slope was determined from this regression as a measure of the rate of thinning for the imaged nanotube.

3.3.2. Comparison to prior ALD conformality results

Using the semi-automated image analysis metrology described above and with these regression methods, experimental data for slope in the ALD depletion region as well as average nanotube wall thickness and diameter in this region were determined (Table 3.1) for 16 different nanotubes fabricated from AAO templates deposited with 10nm of HfO_2 under the same ALD conditions. Slope measurements were quite repeatable amongst the set of 16 nanotubes, with an average slope of around -0.020 with a standard deviation of 0.002 (or 10%). These results are apparently the first time such slopes to indicate ALD depletion effects have been reported, suggesting that our methodology provides a valuable approach for nanotube metrology in general and for understanding the consequences of ALD process chemistry and conformality in particular.

nanotubes	slope
1	-0.021
2	-0.019
3	-0.021
4	-0.021
5	-0.020
6	-0.016
7	-0.016
8	-0.024
9	-0.020
10	-0.022
11	-0.021
12	-0.020
13	-0.020
14	-0.018
15	-0.017
16	-0.017
average	-0.020
std dev	0.002

Table 3.1 experimentally measured slopes for 16 separate nanotubes. Experimental measurements of the slopes can be compared directly to values derived from two literature models.[44, 46]

As an alternative, we have compared these results to those generated by kinetic simulations/models reported by Gordon et al.[46] and Elam et al.[44]. We recreated each of these mathematical models for the parameters describing our experimental conditions. The areal density of reactive sites [46] was taken as $2.5*10^{18}$ sites/m^{-2}. A sticking coefficient of 100% was used for both models (sticking coefficients are fixed in Gordon's model but adjustable in Elam's model). We treated the case of a cylindrical nanopore with a 60nm diameter and 4μm depth, with the experimentally measured deposition rate of 0.1nm/cycle.

Gordon's model provides the depth of coverage for a single cycle (see equation 3.3).

In order to obtain a slope it was necessary to iterate the model, with each cycle encountering a smaller diameter for the ALD-covered nanopore. This iteration allowed us to simulate the entire 100 cycles of our ALD experiment. Since gas kinetic flow within the nanopore is strictly molecular flow, the rate of thinning depends only on the ALD process parameters, not on the pore dimensions or number of ALD cycles. We determined the slope expected for the ALD depletion region from Gordon's model to be 0.0196, in very good agreement with our experimentally observed value of 0.020.

Elam's Monte Carlo model has fewer assumptions and actually simulates

molecular flow within a nanopore assuming random walk behavior of precursor molecules. The nanopore is split up into an adjustable amount of sectors along its depth. Simulation of ALD was achieved by cycling of the precursor exposures in which each sector could be reacted only once in each cycle. Since, the number of sectors used had some effect on the outcome, the simulation was run multiple times with sector numbers of 25, 50, 75 and 100. The average slope recorded after 5 simulations for each sector number was -0.0186 with a standard deviation of 0.004. Thus, results from Elam's simulations also agree well with slopes in the ALD depletion region determined from our experimental data and image analysis. Our results are apparently the strongest validation currently available for the two models.

3.4. Discussion

Atomic layer deposition, with its capability for atomic-level thickness control and conformal coverage over very demanding 3-D nanoscale topography, is emerging in a major role in nanotechnology. It has already been applied to coating of nanoparticles,[54-57] carbon nanotube electronics,[58-60] energy systems, and interest is increasing in the use of selective ALD.[59, 61] Dozens of different ALD process chemistries have been identified,[62-67] placing a premium on rapid characterization

and understanding of ALD process performance and material quality as realized in nanostructure devices.

The uniqueness of ALD for deposition control is derived from the self-limiting adsorption/reaction of each precursor half-cycle, which leads to both atomic-level thickness control and unprecedented conformality and uniformity. However, in reality the self-limiting behavior is not perfect, leading to depletion effects and process complexity associated with precise precursor doses and interactions between the doses of the different precursors. While the precursor surface reactions are primarily self-limiting and thus account for the high value seen in ALD, it is the deviations from ideal self-limiting reaction that determine the ultimate performance of ALD processes, and the extreme geometries encountered in nanostructure applications push the limits of ALD process performance. The very high aspect ratio of AAO nanopores (depth/width ~50-100) at nm diameters illustrates this point, and it is notable that these aspect ratios are comparable or even higher than state-of-art structures in semiconductor chips today.

Because of this, the development of new metrology approaches to nanostructure fabrication and ALD processes is critical. This is emphasized in the International Technology Roadmap for Semiconductors,[68] which underscores the need to develop

new metrology techniques for sidewall thicknesses in nanostructures, as well as other methods demanded by the new materials and device geometries emerging in nanotechnology. Metrology for novel nanostructures is challenging both qualitatively as well as quantitatively, for ever-smaller dimensions are encountered as new device geometries are invented or achieved. Other high aspect ratio nanopore structures (i.e. track-etched polycarbonate membranes[69, 70]) used for template based synthesis of nanotubes could also benefit from this type of metrology.

3.5. Conclusion

Anodic aluminum oxide templates in combination with the deposition control delivered by atomic layer deposition processes present an attractive route to nanostructure fabrication, but measurement technology to guide and control these processes is challenging. This work demonstrates three relevant metrology advances. First, by dissolution of the AAO template after nanostructure formation, the structures are freed and readily observed in TEM, without need for difficult and painstaking work to create cross-sectional TEM samples. This is useful as part of a metrology strategy whether the intent is to manufacture free nanostructures or nanodevices retained in the AAO template.

Second, an image analysis method has been developed which semi-automates the

extraction of nanotube diameter and wall thickness as a function of depth into the original nanopore. Such a spatial metrology will be important for a variety of applications, because the distribution of wall thicknesses and diameters will likely determine important properties, such as breakdown voltage and leakage current in electrical devices, diffusion through nanotube walls in chemical or drug delivery applications, or sensitivity when nanotubes are used as markers, e.g. as in diagnostic imaging.

Third, we have shown a means to extract parameters from the ALD deposition profiles which reflect the process-limitations of ALD. The deposition regime where nanotube wall thinning is observed reflects the depletion of ALD precursor reaction deep in the nanopores, i.e. a regime which will limit applicability in the more demanding nanostructure geometries. We have derived a characteristic slope parameter from fits to the deposition profiles that may be regarded as measures of the self-limiting performance of a specific ALD process. This can be compared to modeling results and may be attractive as a rapid indicator of ALD process robustness and simplicity, since better self-limiting behavior is desirable. And indeed, rapid feedback of this sort is important given the dozens of ALD process chemistries now of interest to a variety of application areas.

These methods are useful in two domains. All three components are directly relevant to understanding and control of ALD processes and their integration into specific nanodevice fabrication. Indeed, measurements presented here provide what is likely the strongest confirmation to date of existing models for ALD conformality, including both prediction of slopes at deepest penetration point and aspect ratios for which conformality is achieved. In addition, the first two (and perhaps the third) hold value for a broader class of nanostructures, including nanostructures made using AAO templates with electrochemical or other deposition means, and perhaps also using other kinds of templates.

Chapter 4. MIM electrostatic nanocapacitors

This chapter reports the fabrication of Metal-Insulator-Metal (MIM) electrostatic nanocapacitors inside porous AAO templates. The MIM multilayer is deposited by atomic layer deposition (ALD) creating a large, high-density array of cylindrical nanocapacitors. By patterning the top metal electrode, macro capacitors are formed, that contain 10^{10} nanotubes per cm^2. These highly regular arrays have capacitances which are dependent on the depth of AAO pores on to which they are deposited, showing capacitance per unit planar area of 10 $\mu F\ cm^{-2}$ for 1-µm-thick anodic aluminum oxide and 100 $\mu F\ cm^{-2}$ for 10-µm-thick anodic aluminum oxide, as reported for a TiN-Al_2O_3-TiN MIM structure.[71] This chapter will not only report on the electrical characterization of the TiN-Al_2O_3-TiN MIM structure, but also more recent results on TiN-HfO_2-TiN and AZO- Al_2O_3-AZO MIM nanocapacitors.

4.1. Background and motivation

Figure 1.2 shows the current state-of-the-art of energy storage devices that are available. There are three types of storage devices that appear on this graph: electrostatic capacitors, electrochemical capacitors and batteries. Batteries are the most common energy storage devices mainly because they boast very high energy

density. This energy density is stored and released by electrochemical reactions within the batteries electrodes. These redox reactions slow the movement of charge and limit the power density which can be achieved. Batteries have a high energy density, because they store charge within the volume of their electrode.

Electrochemical capacitors (or electric double layer capacitors) store charge in the electrochemical double layer. When compared to batteries electrochemical capacitors have a lower energy density, since charge can only be stored on the electrode surface in the form of an ionic double layer. However, charge-discharge, and therefore power density, is improved in electrochemical capacitors over batteries since electrochemical capacitors do not store charge in slow chemical processes or through phase changes in a material.

Like an electrochemical capacitor, an electrostatic capacitor stores charge only on its electrode interface, and therefore has a low energy density. An electrostatic capacitor is composed of metal electrodes separated by a dielectric material and has even lower energy density when compared to an electrochemical capacitor. This is due to a difference of charge separation within dielectric oxide compared with the electrochemical double layer (10-100nm and 0.3-0.4nm, respectively). However, its charge-discharge is not limited by mass-transport of ions, and therefore it has a higher

power density, which typically is only limited by the external circuit RCs.[71-73]

Advancements in electrochemical capacitors have increased energy densities close to that of conventional battery technology, while maintaining or even increasing device power density. These improvements are seen for electrochemical heterogeneous nanostructured supercapacitors (Figure 1.2). One example of this type of improvement with regards to electrochemical capacitors is shown in Liu et al.[26] for MnO2/PEDOT coaxial nanowires co-electrodeposited in porous AAO. The Templating of these nanowires using porous AAO greatly enhances the surface area of the electrode and is in part the reason for energy density improvements. Likewise, electrostatic capacitors can be improved by simply increasing the surface area available for charge to be stored. Similar to the work of Liu et al.[26] on electrochemical capacitors, electrostatic capacitors can be improved by utilizing the open volume of porous AAO to deposit uniform layers active materials (MIM multilayers). The ultrahigh density of ~10^{10} nanopores/cm^2 of uniformly ordered and hexagonal pores provides a good substrate for area enhancement. This concept is the topic of this chapter and was first reported in the letter by Banerjee et al.[71] (2009) for TiN-Al_2O_3-TiN nanotube capacitors.

There are a few examples in the literature in which nanoporous materials were

used improve electrostatic capacitors. Shelimov et al.[32] used CVD to deposit alternate layers of metallic carbon and insulating boron nitride to create electrostatic capacitors in PAA. Roozeboom et al.[74] used nanoporous n-Si, a ONO dielectric layer and a polysilicon layer to create MIM ultracapacitors. Kemell et al. [75] also used porous Si as a substrate but utilized Al-doped zinc oxide as a top electrode. These examples are seen in Table 4.1 and will be discussed further in the discussion section.

4.2. Materials and Methods

4.2.1. Porous AAO

High-purity, electropolished aluminum foils (99.99% Alfa Aesar) 200 mm thick were anodically bonded to 2-in glass substrates[76] at 380°C using a constant current of 0.7 mA. This critical step prevents cracking of the AAO layer during subsequent processing. AAO pores were then formed on the exposed aluminum surface. The as-processed diameter of the nanopores was ~30 nm, but the pores were pore widened to ~50 nm using a weak phosphoric acid etch. Using the two-step anodization technique as described in section 2.2.2. .[41], pore array that varied in depth 0.5 - 10 μm deep with aspect ratios that varied from 10 : 1 to 200:1.

4.2.2. Deposition and patterning of TiN-Al_2O_3/HfO_2-TiN MIM capacitors

Bottom electrode deposition of TiN by ALD, using tetrakis-dimethyl amido titanium (TDMAT) and NH_3, was carried out in a viscous flow reactor furnace at 175ºC. TiN resistivity of 19 mV-cm was obtained for planar films deposited at this temperature. This value is higher than those reported in the literature and could be a result of the low deposition temperature used in the current scheme[77]. The deposition rate was ~0.16 nm per cycle, yielding a 6.7-nm film (measured using spectroscopic ellipsometry on silicon) for a 40-cycle process. The wafer was then transferred to an ultrahigh-vacuum reactor, described in detail elsewhere.[78]. Before deposition of the ALD Al_2O_3 insulating interlayer, the transfer times were kept to less than 5 min. Trimethyl aluminum and H_2O were used as precursors to deposit Al_2O_3 at 250ºC at a deposition rate of 0.11 nm per cycle to form a 7-nm-thick insulating layer. In the case of HfO_2 dielectric, films were deposited by ALD in a hot-wall stainless steel flow tube ALD reactor, described elsewhere.[79], the insulator thickness measured 7nm. Top electrode deposition was carried out in the furnace reactor, again by depositing a 9.3-nm-thick layer of TiN. Together, the three-layer MIM structure should be ~23 nm thick, that is 46 nm in total, filling nearly completely the 50-nm nanopore diameter.

To form capacitor areas, 500-nm-thick aluminum was deposited on the MIM

nanocapacitors in an electron-beam evaporation chamber. Standard photolithography and masking steps were used to pattern the capacitor areas. Wet etching of the electron-beam deposited aluminum was done by Transene-A at 55ºC, followed by top electrode TiN etching using NH_4OH: H_2O_2 : DI water (3 : 2 : 100) at room temperature. This yielded 70 'dot' capacitors, each with an area of 0.01267 mm^2. Each such 'macro' capacitor connected to ~$1x10^6$ nanopore MIM structures in parallel.

4.2.3. Deposition and patterning of AZO- Al_2O_3-AZO MIM capacitors

Bottom electrode deposition of aluminum doped zinc oxide (AZO) by ALD, using diethylzinc (DEZ), trimethyl aluminum (TMA) and water, was carried out in a BENEQ TFS-500 ALD reactor at 150°C. One supercycle of AZO is composed of 10 cycles of DEZ and water followed by one cycle of TMA and water. The deposition rate was 2.1 nm per supercycle, yielding a 10.5 nm film (measured using spectroscopic ellipsometry on silicon) for a 5 supercycle process. In the same reactor, 2nm of titanium oxide (TDMAT and water) was deposited as an etch stop for the top electrode wet etch. Trimethyl aluminum and H_2O were used as precursors to deposit Al_2O_3 at 150°C at a deposition rate of 0.1 nm per cycle to form a 6-nm-thick insulating layer. Top electrode deposition was then carried by depositing a 100-nm-thick layer of AZO.

Standard photolithography and masking steps were used to pattern the capacitor areas. Wet etching of the AZO was done in a 1:1000 HCl solution at room temperature for 3 minutes, utilizing the TiO_2 as an etch stop so as not to damage the very thin AZO bottom electrode. This yielded 'dot' capacitors, each with an area of ~$3.5x10^3$ cm^2. Each such 'macro' capacitor connected to $3.5x10^6$ nanopore MIM structures in parallel.

4.2.4. Materials and electrical characterization

Material characterization was conducted using a Hitachi SU-70 analytical SEM. To verify the conformality and composition of the nanocapacitors, the 10-μm-deep AAO template for the TiN-Al_2O_3-TiN capacitors was dissolved in 0.1 M NaOH and MIM nanotubes were collected on a copper grid for TEM analysis using a JEOL 2100F with EDX capability. Electrical characterization was carried out using an Agilent E4980A LCR meter for low-frequency capacitance measurements, an Agilent 4155C for quasi-static capacitance measurements, and an HP 4145B for leakage current measurements.

4.3. Results

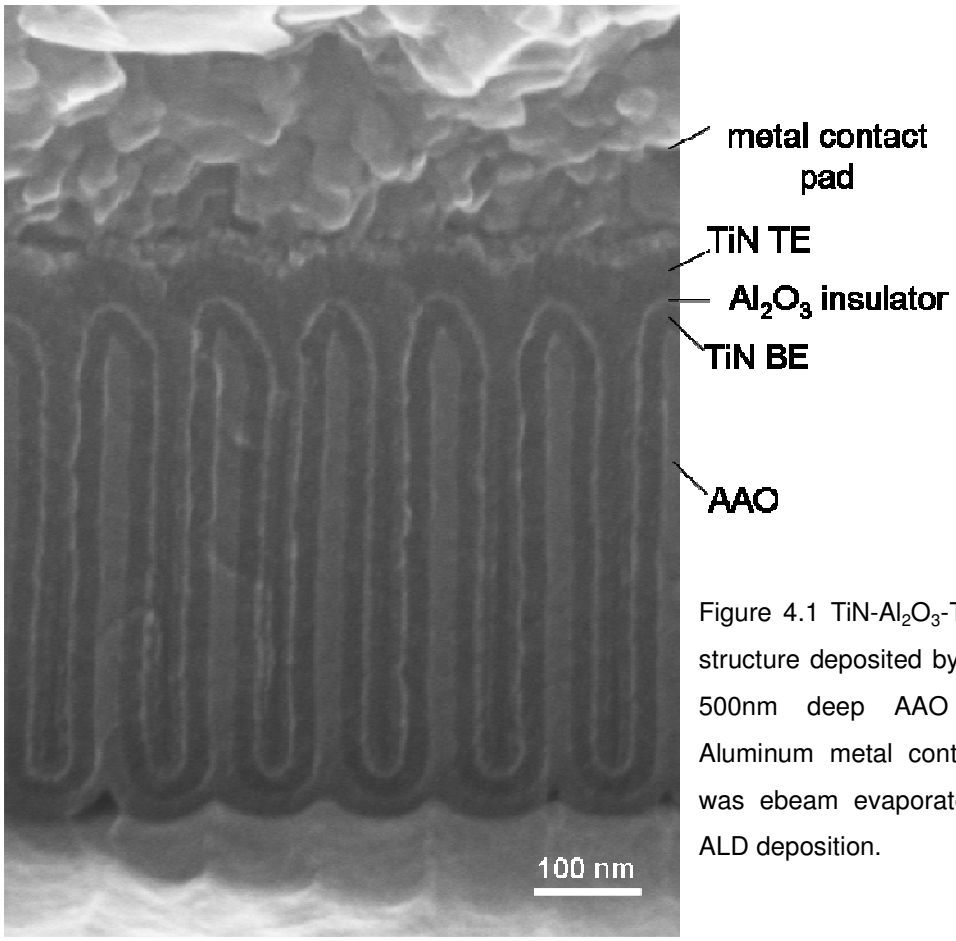

Figure 4.1 TiN-Al_2O_3-TiN MIM structure deposited by ALD in 500nm deep AAO pores. Aluminum metal contact pad was ebeam evaporated after ALD deposition.

4.3.1. Deposition and processing results

MIM capacitor structures are formed by the application of successive ALD layers of metal (TiN or AZO), insulator (Al_2O_3 or HfO_2) and metal (also TiN or AZO) with atomic layer thickness control down to the deepest surface with the porous AAO substrate. A deposition method with excellent conformality in highly nanostructured surfaces, such as ALD, is necessary for this application so that the final electrostatic

capacitor can benefit from all usable space afforded by the porous AAO substrate. Figure 4.1 shows an SEM image of nanopores into which a TiN-Al_2O_3-TiN MIM stack was applied using ALD. Contrast differences in the SEM image delineate the different materials, with the TiN bottom electrode (BE) and top electrode (TE) being the darkest and the ALD- Al_2O_3 insulator and anodic alumina substrate having a brighter contrast. TEM was also utilized to image released MIM nanotubes as seen in Figure 3.5a. EDS line scans for titanium and aluminum (Figure 4.2b) show peaks characteristic of the three concentric layers within each nanopore, and comply with the geometric assumptions laid out in the nanotube metrology method detailed in chapter 3.

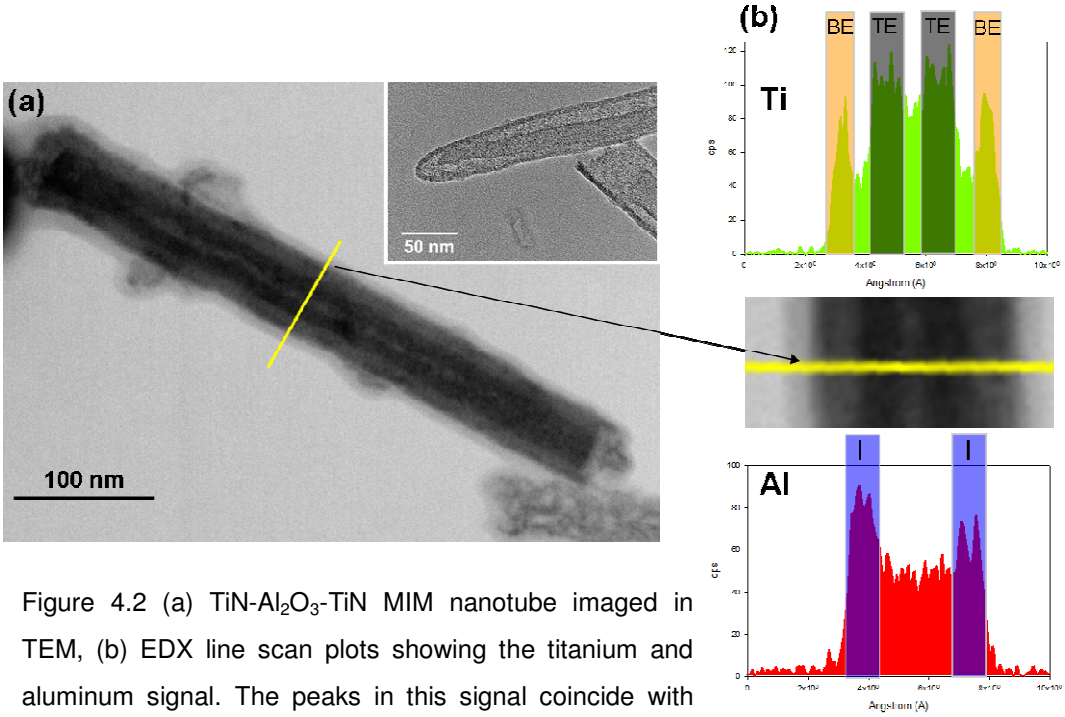

Figure 4.2 (a) TiN-Al_2O_3-TiN MIM nanotube imaged in TEM, (b) EDX line scan plots showing the titanium and aluminum signal. The peaks in this signal coincide with cylindrical nanotube model covered in chapter 3.

Figure 4.3 shows two side by side SEM images of a porous AAO substrate which is deposited with an AZO-Al_2O_3-AZO MIM stack. This sample has been lithographically patterned and etched. Figure 4.3a shows AAO pores that are outside of the macro capacitor area which have only the AZO BE after the 1:1000 HCl solution had etched the AZO TE to define the capacitor area. As can be seen the BE is extremely thin, and it is necessary to take steps to assure it stays intact in order for it function properly as a bottom electrode, carrying charge from the edge of the sample to the capacitor being tested. Utilizing a very thin (1-2nm) TiO_2 ALD layer as an etch stop in addition to the Al_2O_3 insulator assured that the etching solution would stop

etching after defining the TE areas. Figure 4.3b shows the MIM stack still intact with the AZO BE and the AZO TE separated by the thin dielectric of 6nm Al_2O_3 and 2nm TiO_2.

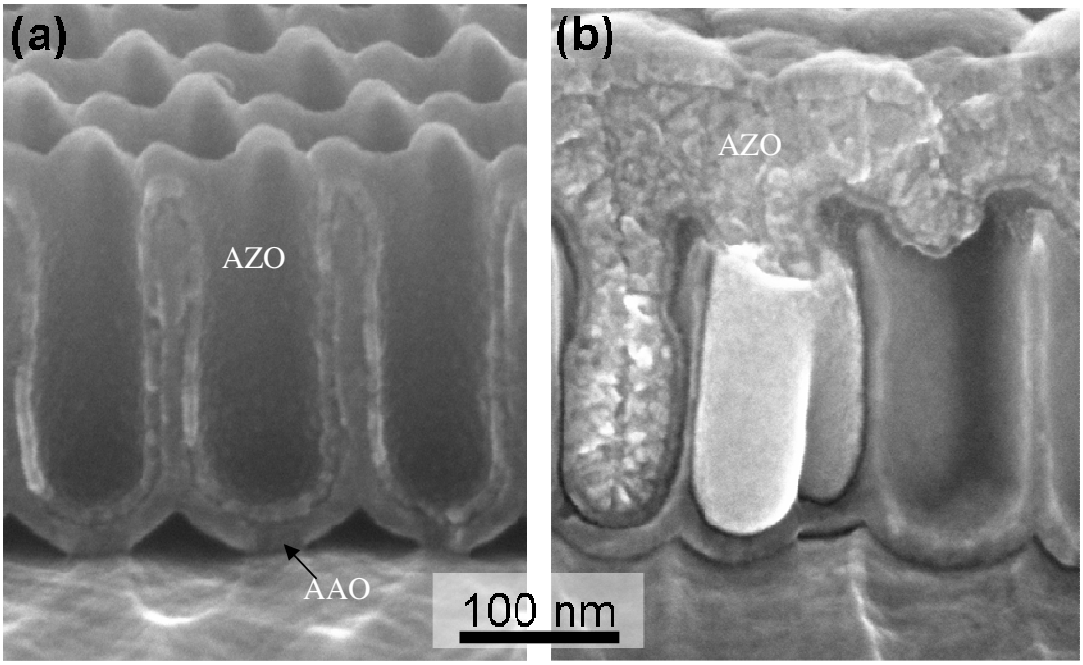

Figure 4.3 AZO- Al_2O_3-AZO nanocapacitor cross-section images (a) outside of patterned capacitor area with only bottom AZO and (b) inside patterned capacitor area with top electrode still intact.

4.3.2. Capacitance

The schematic in Figure 4.4 shows how the capacitors were hooked within the circuit after patterning. The bottom electrode was contacted on the edge of the sample though the aluminum substrate. This was possible since all samples were made so that

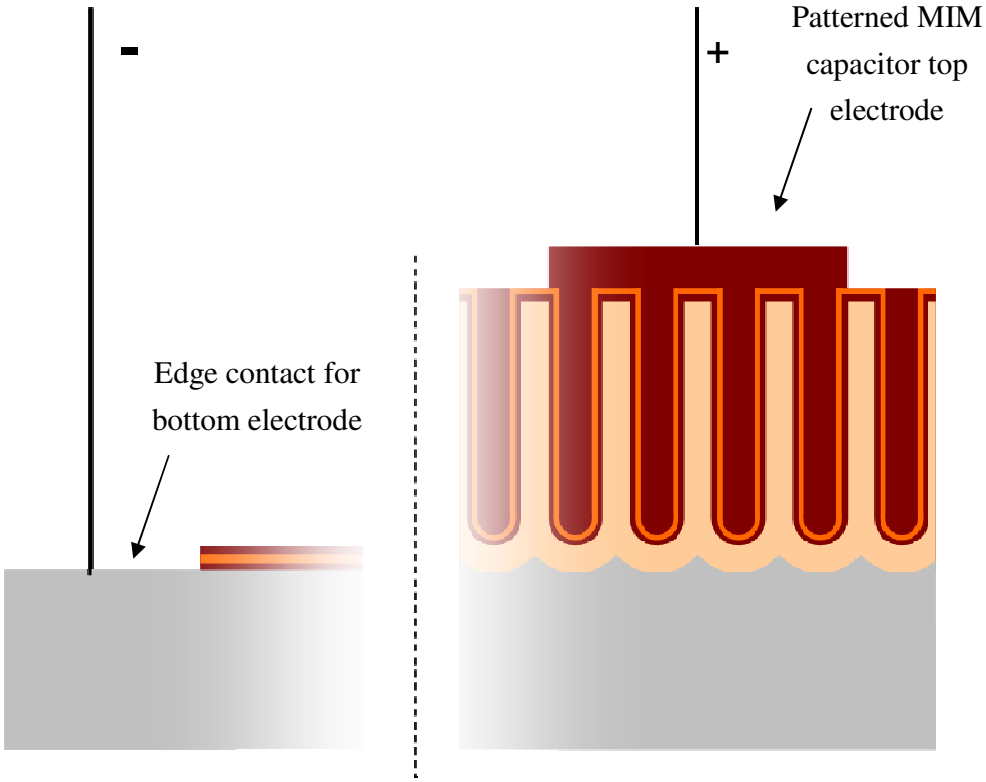

Figure 4.4 Capacitor schematic showing MIM layers inside AAO pores with a patterned top capacitor. Back contact is made ath edge of the wafer by contactin substrate aluminum.

the porous AAO material was confined to the center of the substrate, leaving the edges with the aluminum exposed.

The capacitance of the individual 'macro' capacitor structures were measured using an Agilent E4980A LCR meter. Low frequency measurements (20Hz) were used to measure capacitance since the capacitors for energy and high power applications operate in few tens of Hertz. Frequencies higher than 100 Hz resulted in

notable dispersion, with decreasing capacitance as frequency increased. Capacitance measurements are given in Effective Planar Capacitance (EPC), which is the capacitance per planar area on a sample. For the TiN-Al_2O_3-TiN capacitors in 1µm and 10µm pores EPC values of 13.4±2.1 µF cm^{-2} and 99.1±17.5 µF cm^{-2} were obtained, respectively. For the TiN-HfO_2-TiN capacitors in 1µm pores an EPC value of 16 µF cm^{-2} was obtained. For more recent AZO-Al_2O_3-AZO EPC values for 500nm, 1µm and 2µm are as follow: EPC(500nm) = 9.4±0.5 µF cm^{-2}, EPC(1µm) = 13.6 ±1.5 µF cm^{-2}, and EPC(2µm) = 16.5±2.6 µF cm^{-2}.

To verify the above capacitance measurements the nanocapacitors were quasi-statically probed for capacitance by measuring the displacement current during a voltage ramp step and accounting for the excessive dielectric leakage. The in 1µm and 10µm TiN-Al_2O_3-TiN capacitors were measured and EPC values of 13.4±2.1 µF cm^{-2} and 99.1±17.5 µF cm^{-2} were obtained for samples, respectively. The good correlation of the results of these two independent techniques confirms the high capacitance of these structures at low frequencies.

4.3.3. IV measurements

Current–voltage measurements were also made for the nanocapacitors. For the

TiN-Al_2O_3-TiN capacitors, initial leakage currents were high. Two treatments of the AAO surface reduced leakage dramatically to $5x10^{-9}$ A cm^{-2} at 3 MV cm^{-2} (where the current density is relative to the full area of the capacitor), values comparable to those previously reported.[80] The first treatment was a pore widening step (1 : 1 NH_4OH : DI water for 1,000 s), which increased pore diameters to 80 nm. The second treatment added an ALD Al_2O_3 barrier film, which reduced the pore diameter to 50 nm before the MIM stack was deposited. The improved leakage may signify chemical passivation and perhaps nanostructural smoothing of the AAO surface. Typical leakage characteristics for the AZO-Al_2O_3-AZO capacitors were ~$6x10^{-8}$ A cm^{-2} at 3 MV cm^{-2} without any ALD Al_2O_3 pre-film applied to the substrate. Current-voltage characteristics in terms of dielectric breakdown will be discussed below.

4.4. Discussion

4.4.1. Performance

The effective planar capacitance (EPC) is defined as the capacitance per planar area and is used here to compare the performance between different MIM structures. EPC can be estimated knowing the dimensions of the porous AAO structure and the thicknesses of the bottom electrode and insulator layers using this equation:

$$EPC = D * \frac{2\pi k\varepsilon_o L}{\ln(b/a)} + \frac{k\varepsilon_o}{t_i} \tag{4.1}$$

where D is the pore density, k is the dielectric constant of the insulator, ε_o is the permittivity of free space, L is the pore depth, and t_i is the thickness of the insulator. Constantans a and b depend on the thicknesses of the ALD layers and the radius of the pores as follows: $a = r_p - t_i - t_{BE}$, $b = r_p - t_{BE}$. For the dimensions of the porous AAO template utilized in this work, with an interpore spacing of ~105nm with hexagonal pore ordering, the pore density is ~10^{10} nanotubes per cm^2. Figure 4.5 shows schematically the relevant dimensions for the EPC calculation. The first term in equation 4.1 relates to the cylindrical capacitance of each pore and the second term estimates the contribution of the top surface and the bottom of the pore. For pores depths larger than 1μm, the second term becomes negligible with respect to the first.

For the TiN-Al_2O_3-TiN 1µm and 10µm capacitors, theoretically EPC values are 13.2 µF cm^{-2} and 123 µF cm^{-2}, respectively, and are in good agreement with the experimentally measure values of 10 µF cm^{-2} and 100 µF cm^{-2}, respectively (calculation used t_i = 7nm, t_{BE} = 6.7nm, $k_{alumina}$ = 7.6). HfO_2 has a higher dielectric constant than Al_2O_3 (k_{HfO2} ~ 14, k_{Al2O3} ~ 7.6) so its estimated EPC value is a little higher at 18.8 µF cm^{-2}, which also is in pretty good agreement with the experimentally measured value of 16 µF cm^{-2}. For the AZO-Al_2O_3-AZO theoretically EPC valu1es are: EPC(500nm) ~9.3 µF cm^{-2}, EPC(1µm)~17.4 µF cm^{-2} and EPC(2µm)~33.8 µF cm^{-2}. While the theoretical EPC value for the 500nm pore is very close to the experimentally measured value, the measured values for the 1 µm and 2 µm pore capacitors are lower than theoretical, at EPC(1µm) = 13.6 ±1.5 µF cm^{-2}, and EPC(2µm) = 16.5±2.6 µF cm^{-2}. This is attributed to the lack of step-coverage of the ALD films deposited with the BENEQ TFS-500 ALD reactor. This can be corrected by increasing exposure times for each precursor during ALD cycling, enabling time for full saturation of surface at the deepest parts of the pores. Unfortunately, the reactor in its current configuration dose not allow for longer exposures.

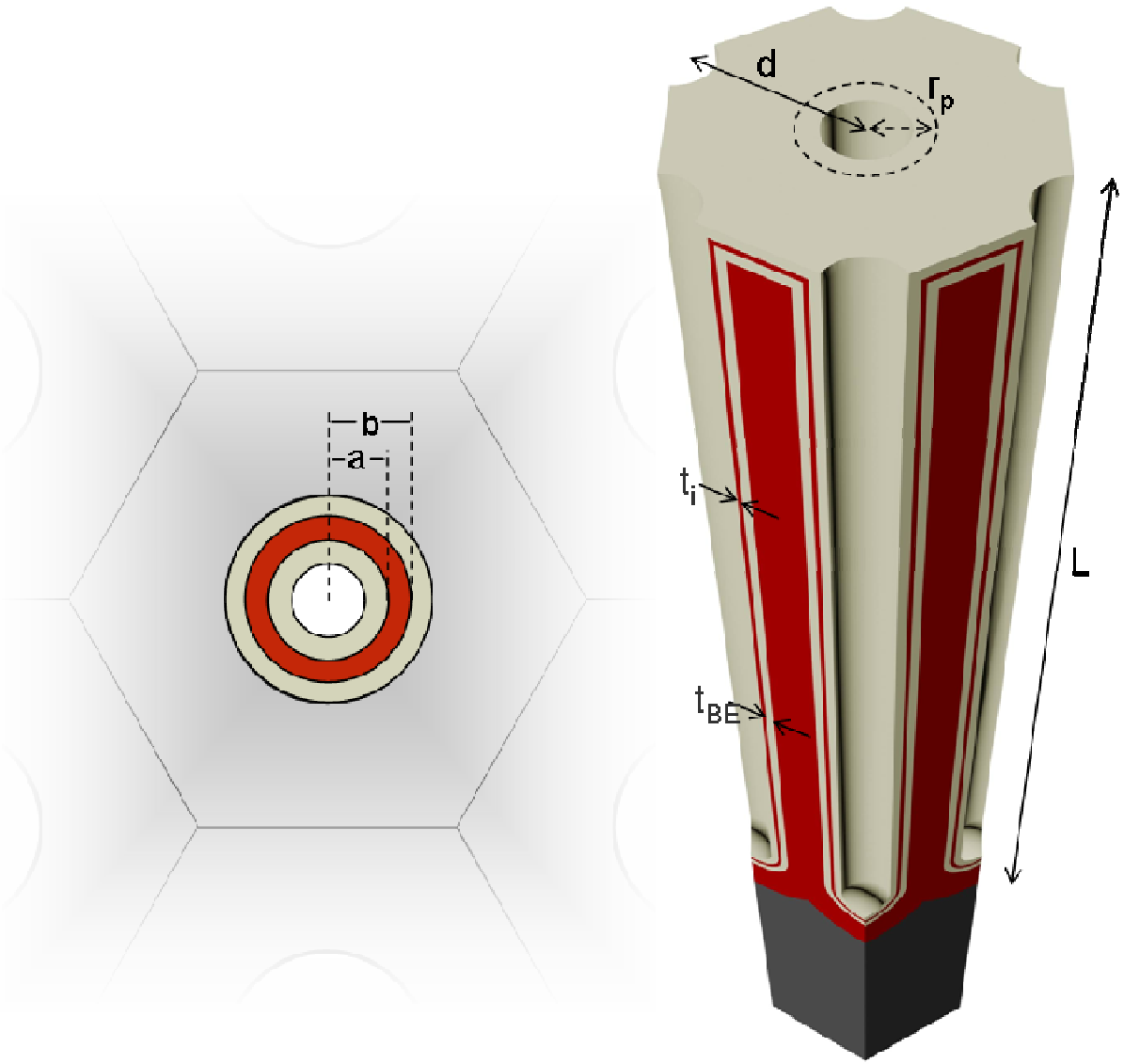

Figure 4.5 Important dimensions concerning theoretical calculation of the Effective Planar Capacitance (EPC) equation

Table 4.1 compares the porous AAO MIM capacitors EPC and capacitance per unit pore volume with similar MIM devices in the literature. This table was published in 2009[71], and shows that at the time of publication our AAO MIM technology had an improved EPC by a factor of 2 when compared to other reported values for a similar MIM device. The closest value came from Klootwijk et al.[81] who fabricated capacitors in Si-trench pores 30μm in depth and 1.5μm in diameter. These capacitors were made by an MIMIM multilayer, whose two stacked capacitors were measured in parallel. EPC values for these capacitors measured at 10kHz, were ~44μF/cm^2.

Our unreported capacitors made with TiN-HfO_2-TiN MIM stack, with similar film thickness and porous AAO have an EPC value of ~16μF/cm^2. EPC value is increased by 60% higher than sample A1 by increasing the dielectric constant of the insulator from k_{Al2O3} ~ 7.6 to k_{HfO2} ~ 14. Figure 4.6 shows the plotted EPC values as a function of pore depth for Al_2O_3 and HfO_2 (r_p = 60nm, t_{BE} = 7nm, t_i = 7nm).

There are three ways to improve the EPC values of these capacitors. One way is to improve the quality of the dielectric, moving to high-k dielectric like HfO_2 (Figure 4.2). Another is to maximize the surface area and open pore volume available to

deposit the MIM layers. This can be done by maximizing the pore diameter to the largest extent before the porous AAO layer collapses. (for 40V, oxalic acid pores ~80-90nm), and maximizing pore depth ($L > 60\mu m$). As seen from the 1 µm and 2 µm AZO-Al_2O_3-AZO samples from above, if the ALD deposition is not adjusted to deposit deep into these pores you cannot benefit from full surface area enhancement provided by porous AAO. Thus, the third and most challenging way to improve EPC is to push the deposition limits of ALD to deposit into deeper pores. Maximizing the pore diameter is a critical adjustment to the template, since it not only benefit the surface area enhancement, but also lowers the diffusion limitations of ALD deposition, allowing for deeper penetration of the MIM layer (see section 3.3.2.).

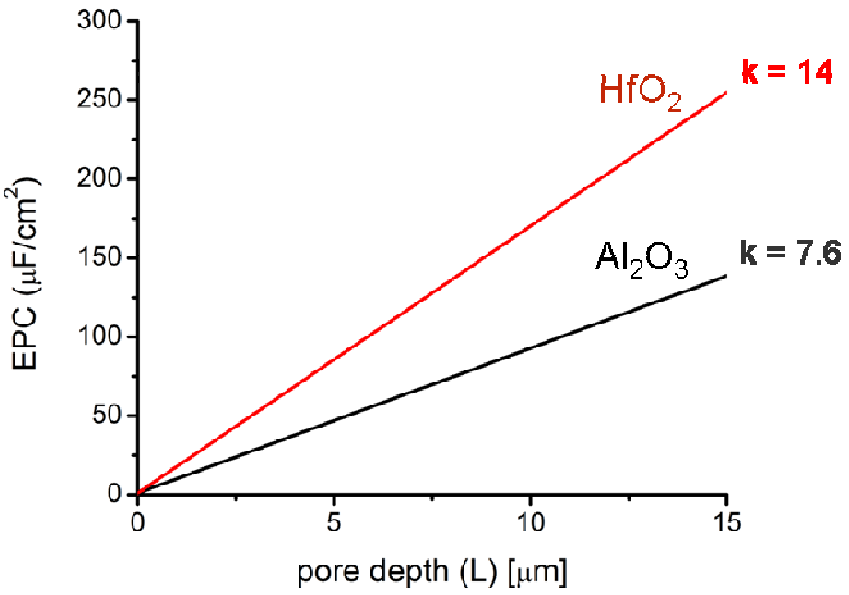

Figure 4.6 Theoretical EPC values plotted as a function of pore depth (r_p = 60nm, t_{BE} = 7nm, t_i = 7nm) for HfO_2 and Al_2O_3 using equation 7.

	Reference	Template	Film deposition technique	Metal	Insulator (Thickness)	Metal
Nanoporous	Current work (sample A10)	AAO 0.3 M oxalic acid	ALD	TiN	ALD Al_2O_3 (6.7 nm)	TiN
	Current work (sample A1)	AAO 0.3 M oxalic acid	ALD	TiN	ALD Al_2O_3 (6.7 nm)	TiN
	Shelimov *et al.*[4]	Commercial Whatman™ Anodisc	CVD	Amorphous C	BN (70 nm)	Amorphous C
	Sohn *et al.*[5]	AAO 0.3 M H_2SO_4	CVD	Al	Barrier layer Al_2O_3 (27 nm)	Carbon nanotubes
Microporous	Klootwijk *et al.*[6]	ULSI Si trench	ALD	TiN	ALD Al_2O_3 (10 nm)	TiN
	Kemell *et al.*[2]	Porous Si	ALD	Si	ALD Al_2O_3 (50 nm)	ZnO : Al
	Roozeboom *et al.*[3]	Porous Si	CVD	Si	ONO (30 nm)	Poly-Si

AAO, anodic aluminium oxide; ULSI, ultralarge scale integration; ALD, atomic layer deposition; CVD, chemical vapour deposition; ONO, oxide-nitride-oxide.

	Reference	Pore diameter	Pore depth (μm)	Equivalent planar capacitance (Frequency)	Capacitance per unit pore volume (F cm^{-3})
Nanoporous	Current work (sample A10)	50 nm	10	100.0 μF cm^{-2} (20 Hz and d.c.)	100×10^{-3}
	Current work (sample A1)	50 nm	1	10.0 μF cm^{-2} (20 Hz and d.c.)	100×10^{-3}
	Shelimov *et al.*[4]	200 nm	50	2.5 μF cm^{-2} (not given)	0.5×10^{-3}
	Sohn *et al.*[5]	30 nm	0.9	174 nF cm^{-2} (100 kHz)	1.9×10^{-3}
Microporous	Klootwijk *et al.*[6]	1.5 μm	30	44 μF cm^{-2} (10 kHz)	15×10^{-3}
	Kemell *et al.*[2]	2 μm	50	2.5 μF cm^{-2} (10 kHz)	0.5×10^{-3}
	Roozeboom *et al.*[3]	2 μm	150	10 μF cm^{-2} (not given)	0.67×10^{-3}

Table 4.1 Experimentally measured slopes for 16 separate nanotubes. Experimental measurements of the slopes can be compared directly to values derived from two literature models.[44, 46]

4.4.2. IV characteristics

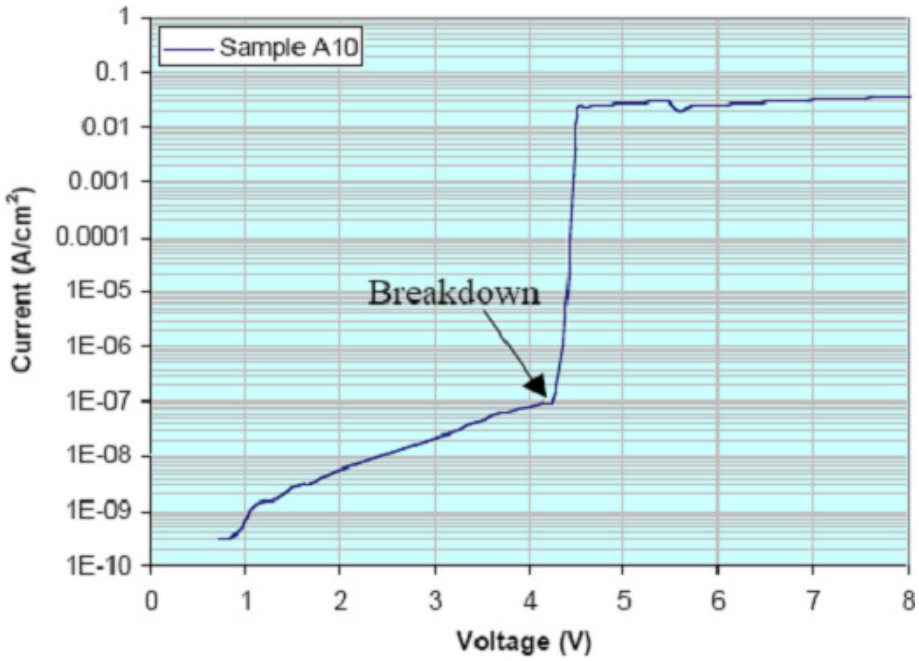

Figure 4.7 Current-voltage sweep for a TiN-Al_2O_3-TiN capacitor showing a breakdown at 4.3 V.

The 1µm and 10µm TiN-Al_2O_3-TiN capacitors showed unusually low field breakdown failing at 4.1±1.9 MV cm^{-1} and 4.6±1.1 MV cm^{-1}, respectively. The similarity of these values, although much lower than Al_2O_3 trench capacitors (12.19 MV cm^{-1})[80], suggests a low field breakdown mechanism independent of nanopore depth, that is, one associated with the nanostructure at the top or bottom of the nanocapacitors or one associated with the properties of the materials. Figure 4.7

shows an example of an IV sweep for the 10µm sample, which breaks down at ~4.3V. Future research will address key materials and process issues for these structures, particularly control of the AAO/ALD and ALD/ALD interfaces involved to optimize important metrics (leakage, breakdown and capacitance). (See future work section 6.2. for further discussion on defect related breakdown for MIM capacitors in porous AAO)

4.5. Conclusion

In conclusion, we have demonstrated operational MIM electrostatic nanocapacitor arrays fabricated with ALD inside AAO nanopores, making use of self-assembly and self-alignment. The TiN-Al_2O_3-TiN nanocapacitors fabricated in 10 µm deep porous AAO achieve equivalent planar capacitances (EPC) of up to ~100 µF cm^{-2}, substantially exceeding previously reported values for nanostructured electrostatic capacitors. The use of HfO_2, a higher-k dielectric, improved EPC values of 1µm TiN-HfO_2-TiN nanocapacitors by approximately ~60%. The use of higher k dielectrics and perhaps higher-aspect-ratio AAO pores may enable higher capacitance values, further boosting the performance of these devices.

Chapter 5. ALD-AAO surface simulations

This chapter covers Matlab surface simulations of ALD onto AAO textured surfaces. First, the motivation for this simulation is given and also the assumptions made at the beginning of the model. Simulated ALD depositions are made on a simulated stripped 1st anodized surface, whose surface is defined by scallops ordered hexagonally surrounded by sharp peaks. The initial surface is created by experimental measurements done by AFM and SEM on AAO structures. ALD deposition rate is experimentally determined by ellipsometry. Topview and sideview surface evolutions images are depicted as a function of ALD film thickness on the surface. From these results calculations on actual surface area and as a function of ALD film thickness are made.

5.1. Background and motivation

As noted in section 3.1.1. ALD is an atomically conformal deposition process because of its discrete cycles which involve self-terminating surface reactions. This makes ALD a suitable method for deposition into nanostructure whose dimension would limit the use of other prevalent deposition processes such as chemical vapor deposition (CVD) and Physical Vapor Deposition (PVD), as long as the ALD recipe is adjusted in terms of exposure time per cycle (see Chapter 3). The topics discussed in Chapter 3 detail the experimental deposition characteristics of ALD films deep into the nanopores of AAO templates. Experimentally, we have also seen interesting

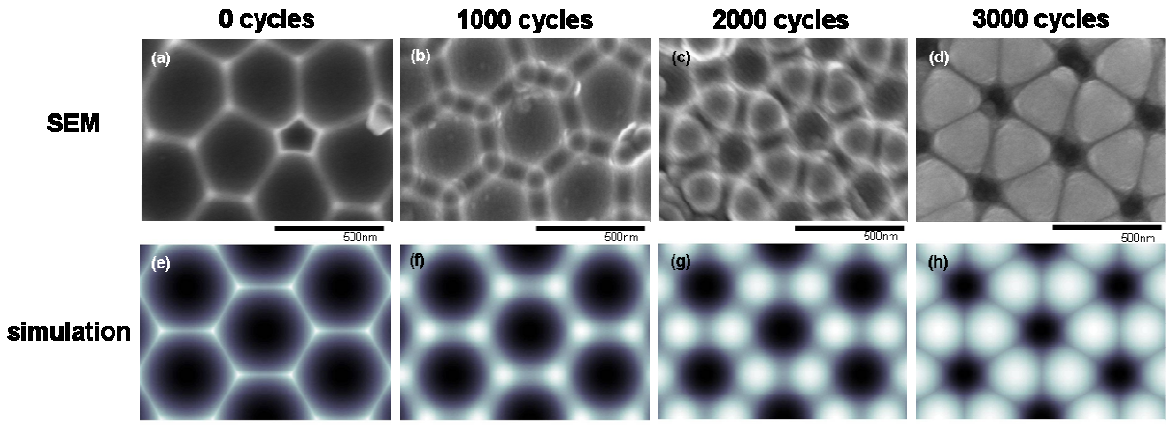

Figure 5.1 (a-d) 1st anodized stripped AAO surface imaged in SEM after ALD TiO_2 deposition of 0 cycles, 1000 cycles (~55nm), 2000 cycles (~110nm), 3000 cycles (~165nm); (e-h) simulation of surface evolution by extruding a model of the initial surface at same rate as the deposition per cycle for ALD TiO_2.[1]

deposition characteristic when depositing on porous AAO and imaging in SEM looking from the topview. An analogous surface to that of the top of porous AAO template is the a 1st anodized surface, which has been stripped of its anodic oxide. This surface is composed of scallops hexagonally arranged, surrounded by sharp peaks that outline the boundaries of the hexagonal pore cells. (see Figure 2.2) Figure 5.1 shows the surface evolution phenomena when depositing on a stripped 1st anodized surface, by imaging the surface from the topview. In order visualize/simulate how these triangular shapes evolve on the surface, I wrote a simple Matlab simulation which is the topic of this chapter.

5.2. Simulation

5.2.1. 1st anodized AAO surface model

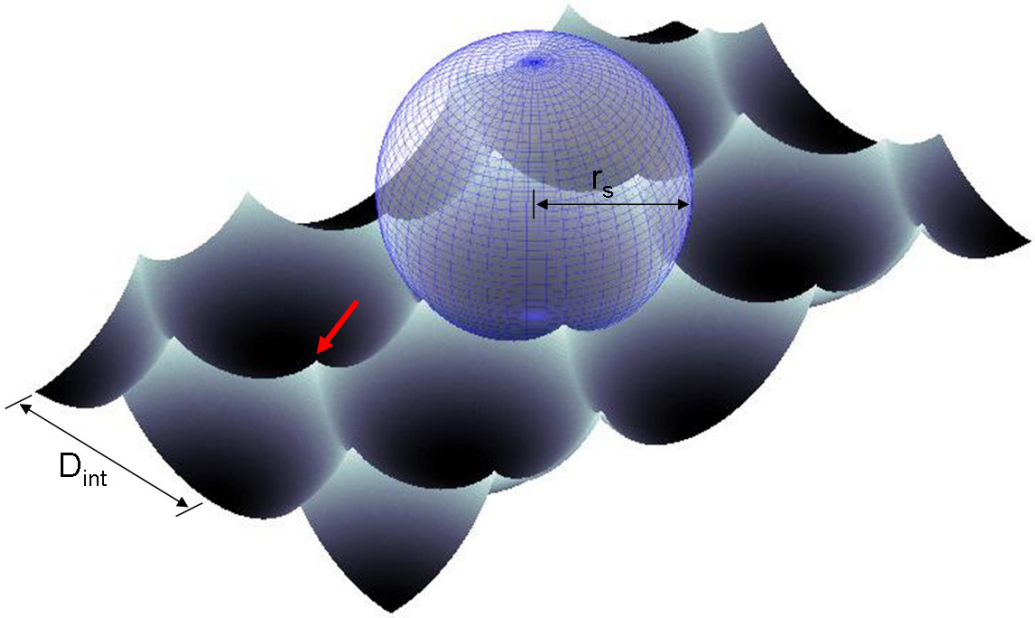

Figure 5.2: 1st anodized stripped AAO surface model; the scalloped surface is made by ordering spheres of radius r_s and spacing them by D_{int} (interpore spacing) in a hexagonal manner.

The spacings and key characteristic dimensions of the scallops on the 1st anodized stripped AAO surface can be measured easily by SEM and AFM characterization. The two most important dimensions used to model the AAO surface were inter pore spacing, D_{int}, and the scallops equivalent sphere radius, r_s (Figure 5.2). The interpore spacing is a well known dimension and is related to the anodization potential by

equation 2.2. For the purposes of this simulation D_{int} is taken as 105nm. The r_s value, which is basically the radius of curvature of the scallop, is a little more difficult to determine experimentally. Instead of determining the r_s directly, we utilized AFM data of an AAO surface to determine the maximum peak height (red arrow in Figure 5.2). This is just the z-height difference between the bottom of the scallop to the top of the peak, which for a AAO aluminum surface anodized at 40V is approximately ~42nm.[1] Knowing this value the surface can be modeled by adjusting r_s until the maximum ideal peak height is ~42nm, which gives a value of r_s ~ 65nm. So, an ideal scalloped surface can be created by spacing hemispheres with radius r_s in a hexagonal array, with inter-sphere spacing of D_{int}, in the closed pack direction, and removing all intersecting data. (see appendix *iii.a* for annotated Matlab code)

5.2.2. ALD deposition assumptions

There are many instances in the literature that cover the strict theoretical modeling of ALD covering topics such as growth per cycle as a function of cycles,[82, 83] initiation kinetics in terms of surface hydroxyls,[84] and Monte Carlo simulations in ultra high aspect nanopores. [44, 85] The simulation that is discussed in this chapter assumes perfect ALD conformality, and doesn't take into account sticking

coefficients[86] or island growth mechanisms[82] which are thought to dominate in the initial cycles of ALD. Instead it uses experimentally determined growth-per-cycle (GPC) and assumes that for each cycle the whole surface will be conformally deposited with a specific amount of material given by GPC of the ALD process being simulated. The use of the experimentally determined GPC value was also used by Elam et al.[44] when simulating ALD deposition in ultra high aspect ratio nanopores.

5.2.3. ALD simulation

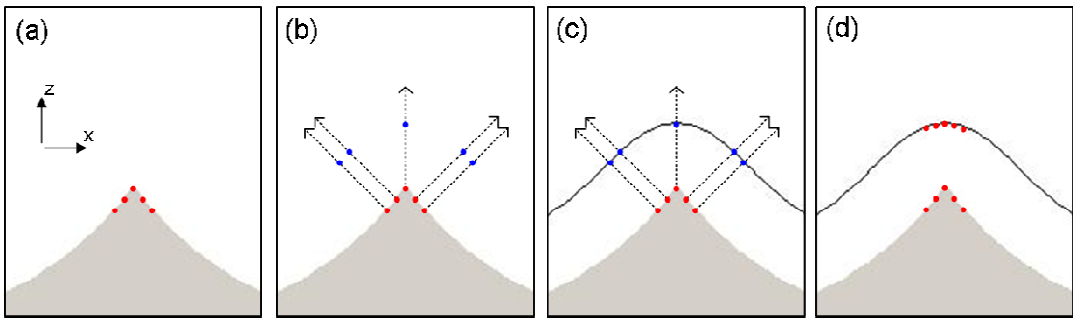

Figure 5.3 (a) five equally spaced data points on the surface of a sharp peak. (b) surface normals are projected out and the data points for the new surface are placed along them using the prescribed GPC value; (c) the new data is fit with the "best fit" line; (d) the fitted line is used to generate more data which is equally spaced in the x-direction.

The initial surface is inputted as three matrices (X,Y,Z) which have the Cartesian coordinates of each data point on the surface. The X and Y data of the surface must be a square grid, meaning the X and Y data points must be equally spaced (this is very easily done using a built in Matlab function *griddata.m*).

Each cycle that simulates ALD has three main steps: (1) compute surface normals for every data point (Matlab function *surfnorm.m*), (2) move each data point along surface normal vector a distance specified by the GPC of the ALD chemistry being simulated (homemade function *distnorm.m*), and (3) fit new surface data with square X-Y grid (Matlab function *griddata.m)*. Figure 5.3 depicts this process step-by-step in a 2D cross-section view to further clarify the steps. Starting with five points on the initial surface (Figure 5.3a), equally spaced on the x-axis, surface normals are determined (dashed lines in b). New data points are moved along each surface normal a distance specified by the GPC of the ALD process being simulated (Figure 5.3b). These new data points are no longer spaced equally on the x-axis, so a new line is fit onto them (Figure 5.3c), and a new set of equally spaced data points are created along this best fit line (Figure 5.3d). In the actual simulation, the data points are spaced no further than 1nm apart, and the GPC is usually smaller than this spacing, so unlike schematic example in Figure 5.3 the simulation proceeds in very small steps to maintain the continuity of the surface.

A simulation was done stating using the methodology described above. The initial surface was gridded in X-Y, with data point equally spaced 1nm. The initial surface was modeled to have the dimensions of a surface made using oxalic acid

chemistry at 40V (0.3M oxalic acid, 40V, 8ºC). The surface D_{int} was set to 105nm and the r_s was set to 65nm, giving a maximum peak height of 43 nm as described above. The actual growth per cycle (GPC) used was 0.1nm/cycle.

5.3. Simulation results and discussion

5.3.1. Comparison of simulation with experimental results

Porous AAO membranes were formed in phosphoric acid with interpore spacings of 450nm and subsequently stripped from the underlying aluminum surface. These templates formed in phosphoric acid were coated in 1000 cycle intervals of TiO_2 ALD which has a GPC of 0.055 nm per cycle. Figure 5.1a-b displays top down SEM images of TiO_2 ALD on top of a stripped PAA surface after anodization in phosphoric acid for 0 cycles, 1000 cycles, 2000 cycles, and 3000 cycles. Since the model that was described above (section 5.2.3.) was done for an initial AAO surface anodized at 40V it cannot be used to compare with these experimental results since the AAO surface were prepared at 160V. From equation 2.2, we know that the interpore spacing, D_{int}, scales with the anodization potential and likewise r_s also scales with potential we can scale the deposition by a factor k = t/Dint. So, the equivalent thickness, τ, is equal to $k_{phosphoric}*D_{sim}$,where D_{sim} is equal to 105nm, D_{exp} is 450nm, and t thickness to be

scaled.

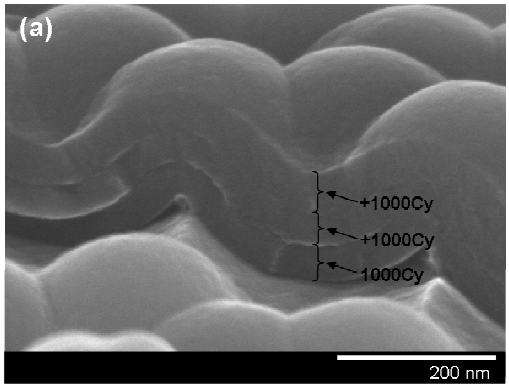

Figure 5.4: (a) SEM ALD deposition of TiO2 on a 1st anodized AAO surface. Three sequential depositions of 55nm (1000cycles) are seen. (b) Simulated ALD surfaces stacked on top of each other, which match well with the SEM result in (a).

(b)

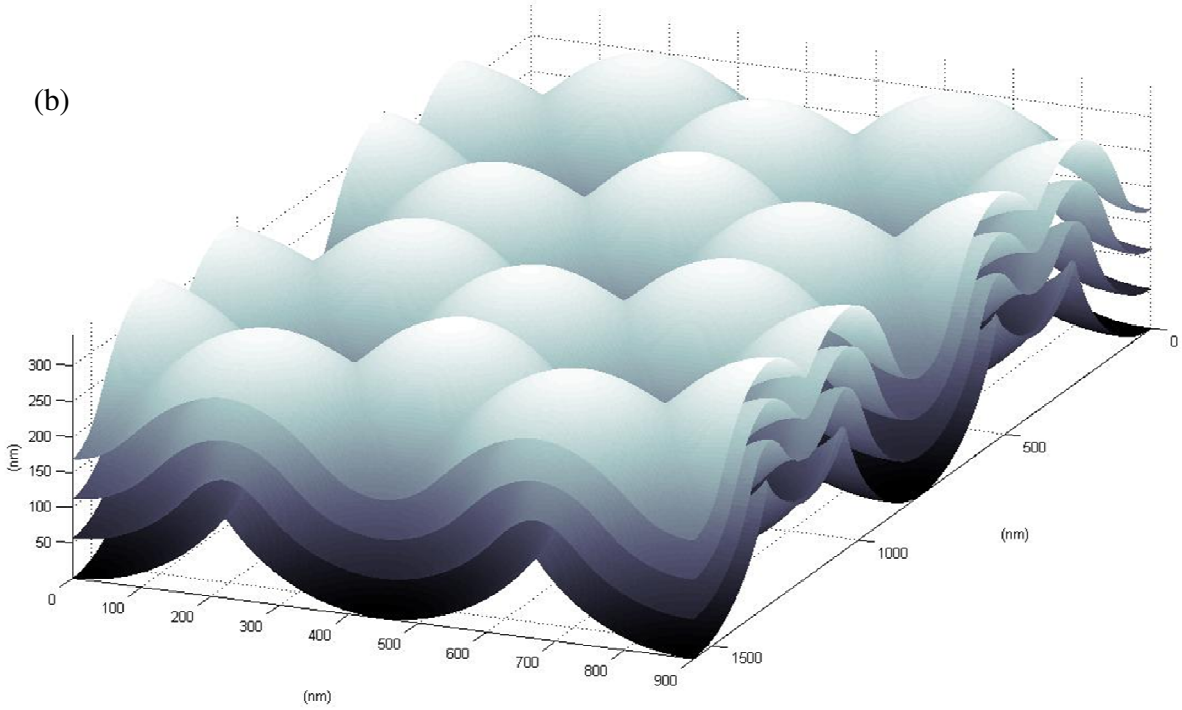

Figure 5.1a-d shows a comparison of topview SEM images and topview of simulation results. The surface evolution mirrors what is seen in the extruded surface simulation. This is an indicator that ALD is depositing in a conformal manner, and

that these island growth seen in SEM are an artifact of the underlying surface and not of some nucleation and growth of particle at the tips of the sharp peaks. Figure 5.4 shows the three layer deposition from a cross-section view for both the experimental deposition and the ALD simulation. The conformality of the ALD deposition is seen for in the SEM (Figure 5.4a) which depicts three discrete layers of equal thickness over the textured surface.

5.3.2. Surface area as a function of film thickness

Using ALD surface simulation results, we can estimate the surface area change as a function of film thickness. The surface area is estimated for a specific area of a model surface which is a representative repeat unit for that surface, by summing the areas of all of the four-sided polygons that make up the surface as defined by the X,Y,Z coordinate data. Starting with the initial surface described in section 5.2.1. an ALD simulation is done for 1000 cycles with a GPC of 0.1nm/cycle. The results are plotted in Figure 5.5, as the normalized surface area (actual estimated area divided by planar equivalent area) as a function of ALD film thickness. The initial surface is estimated to have a 30% larger area than its planar equivalent. As the deposition proceeds the normalized surface does not change appreciably until after ~45nm. After 45nm the

data undergoes exponential decay with a limit of 1. The surface area shoulder seems to coincide with the appearance lines in the film perpendicular to the sides of the hexagonal scallop cells. This is the point in the model where the curvature of the saddle points between the peaks in the 1st anodized surface is completely inverted by the continued extrusion of the surface over the sharp peaks. Further deposition results in the extension of these lines into the center of the scallops further flattening the surface.

Surface area is an important metric when fabricating and testing MIM capacitors on AAO surfaces. The normalized surface area can be used to better estimate the actual surface area of macro capacitors fabricated on AAO. Figure 5.6 shows EPC values for AZO-Al_2O_3-AZO capacitors made on 1st anodized aluminum surfaces along with the EPC values that have been normalized using the surface area calculation made above. The original data shows the same trend as seen in Figure 5.5 and by dividing the normalized surface are by the EPC values, the data is linearized.

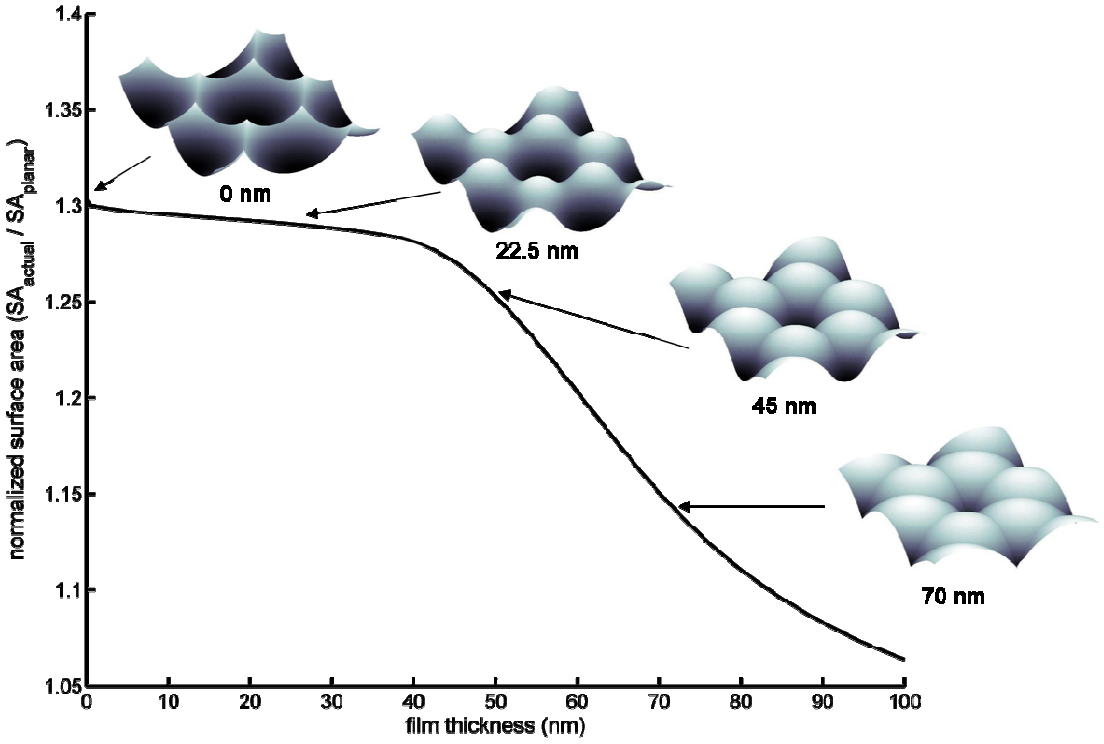

Figure 5.5: Normalized surface area as a function of ALD film thickness.

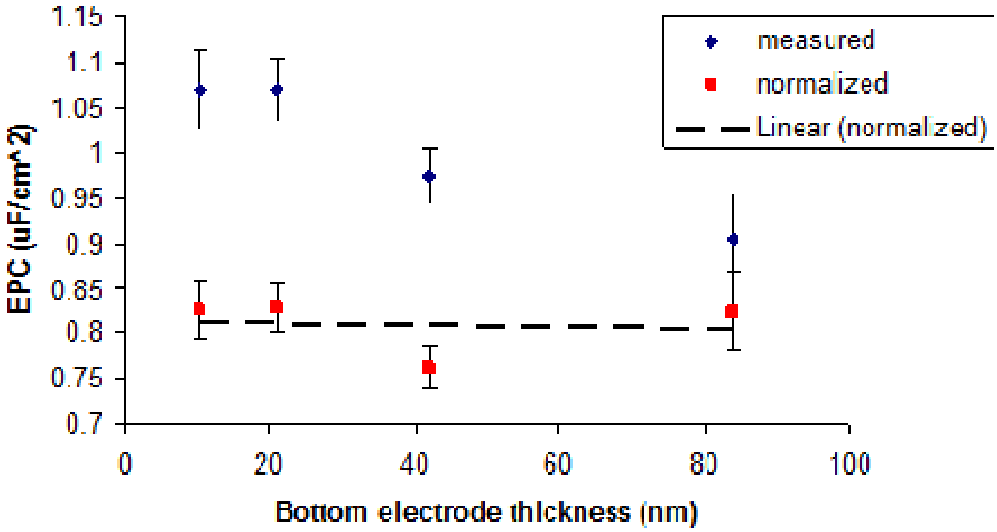

Figure 5.6: EPC plotted as a function of MIM bottom electrode thickness for MIM capacitors fabricated on 1st anodized stripped surfaces (0.3M oxalic acid, 40V, 8C). Red curve has been normalized using surface area factor from Figure 5.5.

5.4. Conclusions

In conclusion, we have demonstrated the usefulness of a simple extrusion model to simulate the surface evolution of ALD deposition on AAO surfaces. A model of a 1st anodized stripped AAO surface was made by calibrating it with dimensions extracted from SEM and AFM scans. The surface was then extruded in a stepwise manor using the experimentally obtaining growth per cycle (GPC) value of the ALD chemistry being simulated. Experimental topview SEM images and simulated top view surface images compared favorably, leading to the conclusion that the appearance of non conformal nucleation and growth is an artifact of the underlying textured AAO surface. Using this model, the surface area enhancement is dependent on deposition film thickness was calculated, and was applied to MIM capacitors made on AAO surfaces to better estimate their actual capacitor area.

Chapter 6. Conclusions and Future work

6.1. Conclusions

The overall goal of this research is to utilize self-assembled porous AAO membranes coupled with conformal deposition of multi-layered thin films using ALD to create nanostructured energy storage devices. Porous AAO benefits from its natural tendency towards self-order, resulting in highly dense and aligned nanopore arrays. Because these nanoporous arrays can be made over large areas by a very simple electrochemical process, they are a very cost-effective alternative when compared to nanostructures fabricated using traditional lithographic techniques. ALD proves to be a deposition method that is uniquely suited for depositing thin-films into the high aspect ratio AAO nanopores because it utilizes self-limiting surface reactions and can be adjusted to compensate for diffusion limitations within the nanoporous membrane.

Our approach is threefold: 1) Build porous AAO substrates, tailoring the dimensions and surface structures to maximize final device efficiency; 2) Deposit ALD layers into AAO nanopores, adjusting ALD deposition parameters to assure conformal coatings to the deepest portions of the pores; 3) Build novel energy devices which can benefit from the surface area enhancement provided by porous AAO and the conformal

thin-films of ALD.

In this thesis, I have developed a nanotube metrology method which assists in characterizing deposition conformality in ultra high aspect ratio nanopores. This was achieved through the use of "nanotube template synthesis", in which porous AAO membrane is first coated by ALD, and then later nanotubes are released by dissolution of the AAO template. Nanotubes were spread on TEM grids, and imaged along their full length. A Matlab script was used to make multiple lines scans perpendicular to the nanotube axis, applying a cylindrical model in order to extract ALD film thickness as a function of depth within the nanopores. The novel aspect of this nanotube metrology method is that it can extract actual film thickness as a function of depth rather than relying on EDX signals scanned from top to bottom of the bulk membrane cross-sections. This metrology has application in improving deposition conformality of ALD and other deposition methods, by offering a quick and reliable feedback to changes in deposition parameters.

Also, in this thesis, MIM electrostatic nanocapacitor arrays were fabricated as a novel energy device that could benefit from high surface area enhancement of porous AAO. ALD multilayer, metal-insulator-metal (MIM) depositions were applied to porous AAO substrates taking advantage of the large open pore volume inherent to

porous AAO. MIM stacks of different materials were made including TiN-Al_2O_3-TiN, TiN-HfO_2-TiN and AZO-Al_2O_3-AZO. TiN-Al_2O_3-TiN nanocapacitors fabricated in 10 μm deep porous AAO achieved equivalent planar capacitances (EPC) of up to ~100 μF cm^{-2}, substantially exceeding previously reported values for nanostructured electrostatic capacitors. The use of HfO_2, a higher-k dielectric, improved EPC values of 1μm TiN-HfO_2-TiN nanocapacitors by approximately ~60%. AZO-Al_2O_3-AZO reflect EPC improvements seen for TiN-electrode capacitors and have the added benefit of being a transparent structure. The use of higher k dielectrics and perhaps higher-aspect-ratio AAO pores may enable higher capacitance values, further boosting the performance of these devices. Further research needs to center around the chemical and structural influences of porous AAO templates on the electrical characteristics of the MIM capacitors, including electrical breakdown, and low field leakage currents.

6.2. Future work – reliability issues for MIM electrostatic nanocapacitors

As reported in chapter 4, MIM electrostatic nanocapacitors were shown to suffer from low field breakdown mechanisms. This low field breakdown is thought to be associated with the characteristic sharp peaks at the top surface of the porous AAO

templates. One key piece of evidence that singles out these top surface peaks is the similar breakdown field seen for both 1µm and 10 µm deep templates (section 4.4.2.), even though 10 µm deep porous AAO has 10x the surface area when compared to 1µm deep porous AAO.

6.2.1. Understanding defect related breakdown on porous AAO

The sharp asperities on the top surface of porous AAO are suspected to be the main cause of low field breakdown. In an ideal hexagonally ordered porous AAO array, pores are surrounded by six sharp peaks that are similar in dimensions. In reality, the peaks vary in size, in particular in the regions of the AAO surfaces that lie between large domains of perfect hexagonal ordering. Figure 6.1 show top surface images of (a) a 1st anodized stripped aluminum surface and (b) a porous AAO template. Bright spots on the surface correlate with regions of disorder which do not have perfect hexagonal packing. Peaks in perfect hexagonal domains are surrounded by three pores/scallops. Along the hexagonal domain boundaries, there are occurrences of peaks that are surrounded by 4 or even 5 pores/scallops. Looking at the sideview in Figure 6.1c-d, peaks that are between pores that are not hexagonally packed are characteristically taller. These sharp peaks in disordered regions should dominate

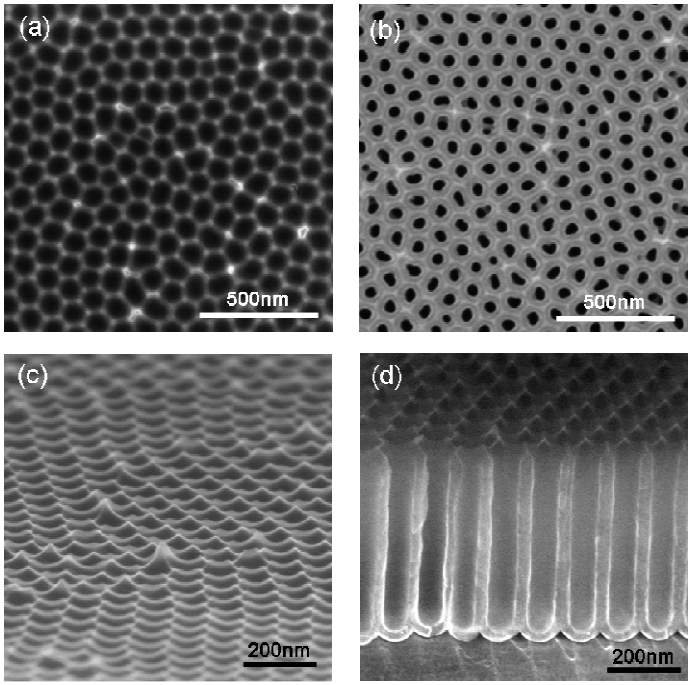

Figure 6.1:, SEM images showing the occurrence of sharp asperities at hexagonal domain boundaries on AAO surfaces, (a) topview image stripped 1st anodized aluminum; (b) topview image porous AAO; (c) sideview image stripped 1st anodized aluminum; (d) sideview image porous AAO.

breakdown characteristics.

One experiment that can clarify this notion would be to fabricate MIM capacitors on the surfaces of both 1st anodized stripped AAO and porous AAO substrates, which have been 1st anodized for different length of time. As explained in section 2.1. there is evolution of domain ordering with respect anodization time. Starting with an electropolished aluminum sample, the porous membrane will self-order over time till the pore ordering finally saturates. Domain sizes at optimum ordering are around ~1-3μm in diameter. So, by varying the 1st anodization time, the density of non-ideal asperities (those not associated with ideal hexagonal ordering) can be controlled and should be reflected in the breakdown field measured during IV sweeps. Weibull probability plots of

statistically significant data sets can be used to determine defect density for each sample[87], and these can be correlated with defect densities extracted from topview surface SEM like the ones seen in Figure 6.1a-b.

6.2.2. Shape evolution of AAO surfaces as related to breakdown

The sharp asperities of AAO surfaces are thought to lower breakdown fields because have a very small radius of curvature at their tips. Since, the surface charge density is related to the radius of curvature by this equation:

$$\sigma = \varepsilon_o U/R \tag{6.1}$$

where σ is the surface charge density, U is the potential and R is the radius of curvature. The surface charge density is inversely proportional to the radius of curvature, so the surface charge density will be highest at any given potential above the areas on the electrode surface with small radius of curvature.

Similar to the experiment proposed in the previous section, MIM capacitors can be fabricated, on an AAO surface, this time varying the deposition thickness of the bottom electrode. Chapter 5 of this thesis describes the surface evolution as a function of ALD film thickness which characterized by the rounding of surface features and the overall flattening of the surface (see Figure 5.5). As the thickness of the bottom

electrode is adjusted the radius of curvature of sharp asperities on the AAO surface will increase, reducing their ability to amplify the electric field. The breakdown field of MIM capacitors should be related to the evolution of the top surface of the bottom electrode which is a function of thickness. It is important to monitor both negative and positive IV sweeps, since the breakdown will vary depending on whether the electrons are injected from the bottom electrode through the tips (lower field breakdown), or through the top electrode (higher field breakdown).[88] Looking at the simulation results in Figure 5.5, it would make sense that the breakdown field would lowest for the thinner electrodes (especially when injecting electrons from the substrate through the sharp asperities, negative bias on bottom electrode). As the thickness of the electrode is increased, the mean breakdown field should shift higher. At certain bottom electrode thickness, the surface peaks are inverted as seen for the 70nm surface of Figure 5.5 (inset), which could lead to a trend where breakdown could increase when the electrons are injected from the top electrode as films get thicker.

6.2.3. Rounding of sharp asperities on porous AAO

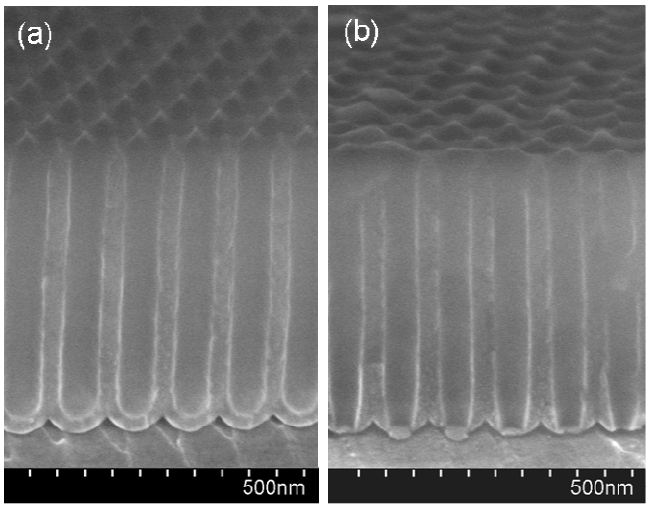

Figure 6.2:, SEM images showing the reduction of sharp asperities the porous AAO top surface, (a) cross-section of porous AAO without RIE etching; (b) cross-section of porous AAO with 60sec Ar/SiCl4 RIE etch.

Improving reliability of MIM electrostatic nanocapacitors built on porous AAO hinges on the removal or rounding of the sharp asperities on the nanostructures top surface. There are two ways this can be achieved: 1) *post-anodization*, by applying some etching technique to the top surface of the AAO, 2) *pre-anodization*, by adjusting the surface of 1st anodized aluminum to eliminate sharp protrusions in the AAO. The most straight forward method of rounding these surface peaks on AAO is with a simple application of an RIE dry etch. This is a common method used to round the sharp edges of trench structures in the semiconductors industry. Figure 6.2 shows a preliminary result for the application of RIE to an AAO structure; (a) a 500nm porous AAO structure which has been pore widened (b) the same structure which has been etched using Ar/$SiCl_4$ RIE chemistry (see appendix *ii.a*

for experimental details).

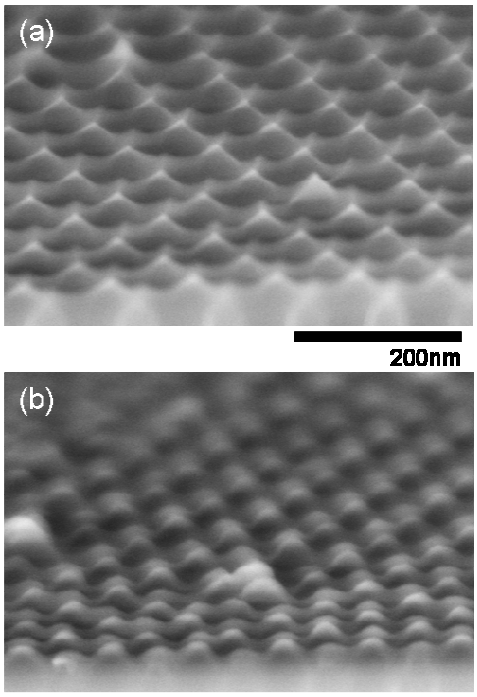

Figure 6.3:, SEM images showing the reduction of sharp asperities the porous AAO top surface, (a) cross-section of a normal porous AAO; (b) cross-section of porous AAO anodized with 20nm ALD Al_2O_3 pre-layer.

Pre-anodization techniques that can influence surface asperities on porous AAO have to reduce surface asperity formation in the early stages of anodization without modifying the nucleation of the ordered pore array. This is not easily done since the surface asperities themselves play a role in transferring order from the 1st anodized scalloped aluminum surface to the growing porous AAO layer (see Figure 2.2). I found that thin ALD Al_2O_3 pre-layer deposited on the stripped 1st anodized AAO surface can influence the final shape of the surface asperities on porous AAO. Figure 6.3 shows two samples, (a) one which was anodized normally and (b) the other which was deposited with 20nm of ALD Al_2O_3 layer prior to anodization. The pre-layer seems to influence the sharpness of the surface asperities making them

rounder, which should enhance electrical reliability. There are two explanations why this technique could influence rounding of surface peaks: (1) the 20nm pre layer protects against the rapid growth of protrusion at the barrier layer stage of AAO growth (Figure 2.2a-b); (b) ALD Al_2O_3 layer changes the chemical surface properties of the top of the porous AAO template resulting in rounder peaks after pore widening. Evidence of the former explanation is seen in the IV curves initial current spike at the onset of anodization is not as large. Evidence of the second explanation is seen in the top surface images before pore widening for both samples which show no apparent difference between surface peaks of either sample.

Appendices

i. AAO

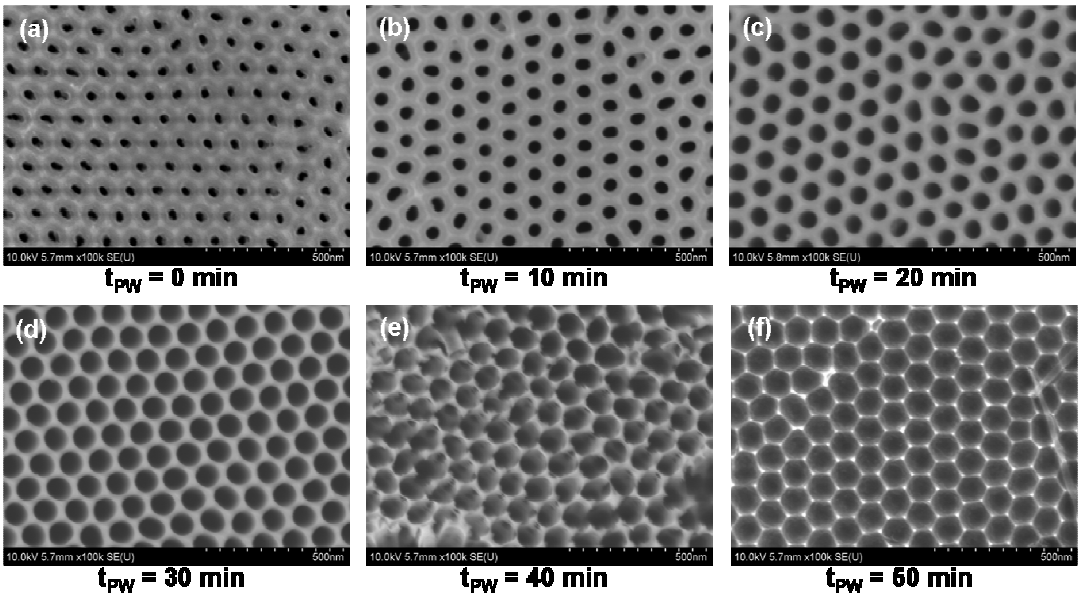

Figure A.1: Topview SEM images of porous AAO membranes pore widened in 0.1M phosphoric acid at 38C for: a) 0min, (b) 10min, (c) 20min, (d) 30min, (e) 40min, and (f) 50min.

a. Pore widening study in phosphoric acid

The pore widening rate of AAP nanopores was found through top view SEM images. Templates were all 1µm deep pores anodized in 0.3M oxalic acid (aq.) 40V 8°C. Pore widening was done in 0.1M phosphoric acid at 38°C was slight agitation from overhead stirrer. Figure A.1 shows top view image of templates that were etched for: (a) 0min, (b) 10min, (c) 20min, (d) 30min, (e) 40min, and (f) 50min. Pore widening time of 40min showed collapse of the structure so samples a-b were

used for determining etch rate.

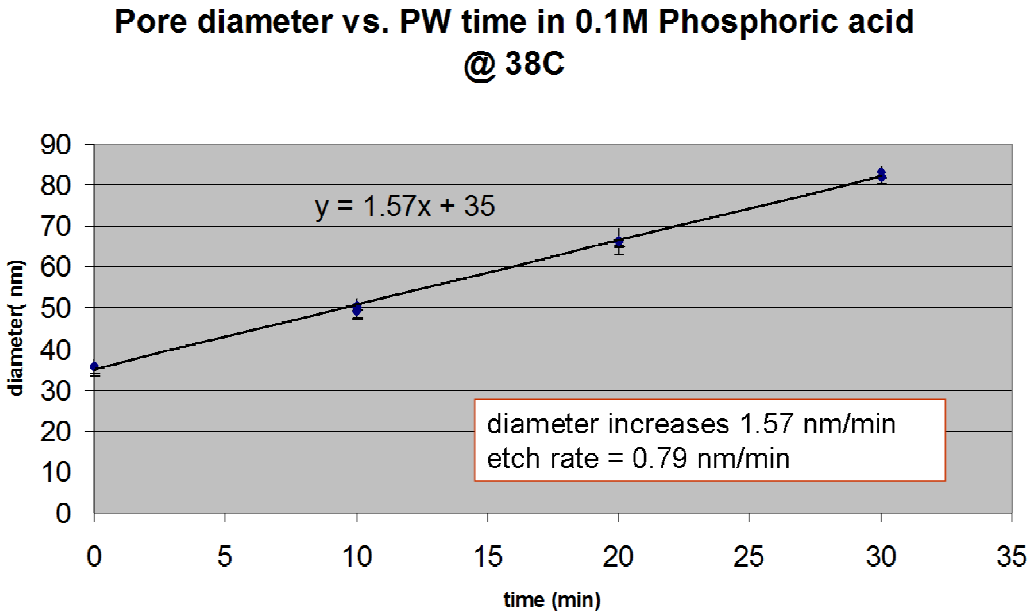

Figure A.2: Pore diameter as a function of pore widening time estimated from topview SEM images

Using 3 images per sample (similar to images in Figure A.1) each image was put through particle analyzing software using *image-j*. First the image had to be scaled using the scale bar. Secondly it had to be converted from grayscale to a binary (black and white image) image, taking care to calibrate the threshold so not to affect the actual diameter of the pores. The built-in particle analyzer software in image-j counted all pores within a set size range; eliminating particles on the edge, and smaller or larger image defects. It also gave the area of each pore in the images. The diameter of each pore was calculated by assuming the pores were circular (area =

πr^2) taking area given by the particle analyzer, and solving for the radius of each pore. The results of this analysis are show in Figure A.2, and show a pore widening rate of ~1.57nm/min (equivalent to an AAO etch rate of ~ 0.79nm/min).

The above results are close reported literature values for this AAO process; the y intercept of the linear trend gives an initial pore diameter of approximately 35nm[14]. Using other data outputted by the image-j particle analyzer, you can estimate other metrics involving porous AAO, such as pore density, pore circularity, and interpore spacing.

b. Sample holders

Anodization sample holders were custom made so that results would be consistent from sample to sample. They also isolate the AAO material to the center of the samples, allowing for contact to AAO devices at the edge or back of sample. Figure A.3 show sample holders for (a) 16x16 mm Al foil samples, (b) for 2in anodically bonded Al/Glass wafers. The inset of Figure A.3 a shows a small Al foil sample after anodization.

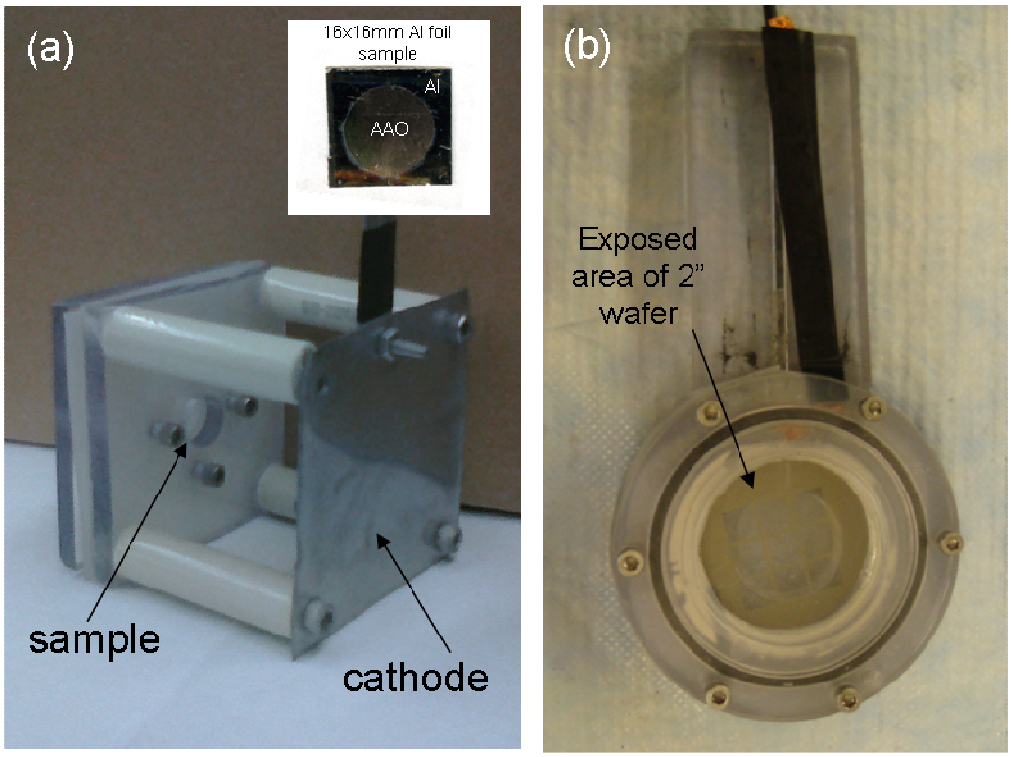

Figure A.3: Custom sample holder for anodization of aluminum samples: (a) small sample holder for 16 x16 mm experimental samples, inset small aluminum sample with AAO. (b) 2in wafer holder for anodization of larger samples.

ii. MIM electrostatic nanocapacitors

a. Ar/$SiCl_4$ RIE of top surface peaks on porous AAO

The porous AAO template was anodized for 415sec at 40v in 0.3M oxalic acid at 8°C which produced a template with 500nm deep pores. Pore widening was done at room temperature for 500sec in 1:1 NH_4OH(28%) aq. Dry etching was done in an Oxford ICP Etcher with these recipe settings: 20°C, 10sccm Ar, 7 sccm $SiCl_4$, 60W electrode power, 350W ICP power, 3.5mTorr, 60sec.

iii. ALD surface simulations

a. ALDsurface.m Matlab code

```
Function ALDsurface
%%%%%%%%%%%%%%%%%%%%%%%%%%%%%%%%%%%%%%%%%%%%%%%%%%%%%%%%%%%%%%%%%%%%%%%%%%%%%%%
%ALDsurface
%This function simulates conformal stepwise deposition on:
%   1) A user created surface
%       -create a surface saving the X,Y,Z coordinates of all data points
%       within a variable struct entitled 'ALDsurfcycles0.mat'
%       -i.e. save(['ALDsurfcycles0'], 'X', 'Y', 'Z')
%   2) Use surface creation script within this code to create an ideal AAO
%   surface with perfect hexagonal ordering

%   Written by Izzy Perez 7/16/09,
%   isr.perez@gmail.com
%   GW Rubloff group, University of Maryland, College Park
%%%%%%%%%%%%%%%%%%%%%%%%%%%%%%%%%%%%%%%%%%%%%%%%%%%%%%%%%%%%%%%%%%%%%%%%%%%%%%%
```

```
%%%%%%%INPUTS%%%%%%%%%%%%%%%%%%%%%%%%%%%%%%%%%%%%%%%%%%%%%%%%%%%%%%%%%%%%%%%%
%inputs for SURFACE CREATION
n = 400; %sphere grid resolution
ro = 65; %radius of equivalent sphere for scallops (nm)
Dint = 105; %interpore spacing (nm)
grid_spc = 1; % space between grid points (nm) -- 1 for oxalic, 2 for phos

skip = 1;%if =1, uses current surface named 'ALDsurfcycles0.mat'

%inputs for ALD REACTOR
cycles_per_loop = 5; %shortens simulation time be simulating many cycles at a time
dep = .1*cycles_per_loop;%deposition thickness per cycle (nm)
cycles = 10000; %total # of ALD cycles to simulate
datapoints = [5:5:cycles];%array ofcycle numbers for which data should be saved
%%%%%%%%%%%%%%%%%%%%%%%%%%%%%%%%%%%%%%%%%%%%%%%%%%%%%%%%%%%%%%%%%%%%%%%%%%%%%%

%%%%%%%%SURFACE CREATION%%%%%%%%%%%%%%%%%%%%%%%%%%%%%%%%%%%%%%%%%%%%%%%%%%%%%
if skip==1
    %%%%%%%%PRE-EXSISTING SURFACE%%%%%%%%%%%%%%%%%%%%%%%%%%
    %if an initial surface does exsist within the working
    %directory this code will load it into the simulation
    load(['ALDsurfcycles0.mat'])%loads pre-exsisting surface
%     y_shift = Dint/2;
%     x_shift = y_shift*tan(deg2rad(60));
    %%%%%%%%%%%%%%%%%%%%%%%%%%%%%%%%%%%%%%%%%%%%%%%%%%%%%%%%%%%%%%%%%%%%%%%%%%%
else
    %%%%%%%%SURFACE CREATION%%%%%%%%%%%%%%%%%%%%%%%%%%%%%%%%
    %if an initial surface dosen't pre-exsist within the working
    %directory this code will create an initial surface using inputted
    %parameters from above

    rh = (Dint/2)/cos(deg2rad(30)); %radius of hexagon, center to corner

    %creates hemisphere surface bottom half with radius "ro"
    [X,Y,Z] = hemisphere(n,0); %this is an embedded function (see below)
```

```
    X1 = ro*X; Y1 = ro*Y; Z1 = ro*Z;

    %determines which points lie inside hexagon of radius "rh"
    L = linspace(0,2.*pi,7); xv = rh*cos(L)';yv = rh*sin(L)';% creates data for a hexagon
    IN = inpolygon(X1,Y1,xv,yv);%finds which points that make up the hemisphere lie within
the hexagonal cell boundary

    %latches multiple hexagons together to create surface
    y_shift = Dint/2;
    x_shift = y_shift*tan(deg2rad(60));
    X2 = [X1(IN),X1(IN),X1(IN),X1(IN),X1(IN),X1(IN)];
    Y2 =
[Y1(IN),Y1(IN)+2*y_shift,Y1(IN)+4*y_shift,Y1(IN)+6*y_shift,Y1(IN)+8*y_shift,Y1(IN)+10
*y_shift];
    Z2 = [Z1(IN),Z1(IN),Z1(IN),Z1(IN),Z1(IN),Z1(IN)];
    X2 = [X2 X2-x_shift X2-2*x_shift X2+x_shift X2+2*x_shift];
    Y2 = [Y2 Y2-y_shift Y2 Y2-y_shift Y2];
    Z2 = [Z2 Z2 Z2 Z2 Z2];

    %creates rectangular data extraction area and extracts data from this area
    xr = [2*x_shift,2*x_shift,2*-x_shift,2*-x_shift];
    yr = [0,6*y_shift,6*y_shift,0];
    IN2 = inpolygon(X2,Y2,xr,yr);%finds all data points in rectangle
    X3 = X2(IN2);
    Y3 = Y2(IN2);
    Z3 = Z2(IN2);

    %%%%%%%%%%%%%%%%%%%%%%%%%%%%%%%%%%%%%%%%%%%%%%%%%%%%%%%%%%%%%%%%%%%%

    %%%%%%%%%%%%%%%%%%%%GRID SURFACE%%%%%%%%%%%%%%%%%%%%%%%%
    %fits data point with surface made up of data points equally spaced in X and Y
    xti = 2*-x_shift:grid_spc:2*x_shift;
    yti = 0:grid_spc:6*y_shift;
    [XI,YI] = meshgrid(xti,yti);
    ZI = griddata(X3,Y3,Z3,XI,YI);
    X4 = XI;
```

```
    Y4 = YI;
    Z4 = ZI+ro;

    %edge fix
    Z4(end,1:end)=Z4(end-1,1:end);
    Z4(1,1:end)=Z4(2,1:end);
    %%%%%%%%%%%%%%%%%%%%%%%%%%%%%%%%%%%%%%%%%%%%%%%%%%%%%%%%%%

    %save surface
    XN = X4;YN = Y4;ZN = Z4;
    save(['ALDsurfcycles' num2str(0)], 'XN', 'YN',
'ZN','x_shift','y_shift','xti','yti')
end




%%%%%%%%ALD REACTOR%%%%%%%%%%%%%%%%%%%%%%%%%%%%%%%%%%%%%%%%%%%%%%%%%%%%%
for i=[1 cycles_per_loop:cycles_per_loop:cycles]
    %cycle counter
    disp(['cycle #: ' num2str(i)])

    % compute surface normals
    [Nx,Ny,Nz] = surfnorm(ZN);

    % create new surface
    [XN1,YN1,ZN1] = distnorm(XN,YN,ZN,XN+Nx,YN+Ny,ZN+Nz,dep);

    % remove NaN values so that griddata function will not fail
    I = isnan(XN1);
    I = find(I==1);
    disp(['# of NaN''s = ' num2str(length(I))])
    disp('__________________')
    XN1(I) = XN(I);YN1(I) = YN(I);ZN1(I) = ZN(I);

    XN = XN1;
```

```
    YN = YN1;
    ZN = ZN1;

    % save data
    datais = isempty(find(i==datapoints));% if data should be saved this equals 0
    if datais == 0, save(['ALDsurfcycles' num2str(i)], 'XN', 'YN', 'ZN'), end

    % grid new surface
%     xti = 2*-x_shift:grid_spc:2*x_shift;
%     yti = 0:grid_spc:6*y_shift;
    [XI,YI] = meshgrid(xti,yti);
    ZI = griddata(XN,YN,ZN,XI,YI);
    XN = XI;
    YN = YI;
    ZN = ZI;
    ZN(1,1:end) = ZI(110,1:end);
    ZN(end,1:end) = ZI(110,1:end);
end
%%%%%%%%%%%%%%%END CODE%%%%%%%%%%%%%%%%%%%%%%%%%%%

%%%%%%%%%%%%%%%embedded functions%%%%%%%%%%%%%%%%%%%%%
function [X,Y,Z] = distnorm(x,y,z,xn,yn,zn,dist)
%%%%%%%%%%%%%%%%%%%%%%%%%%%%%%%%%%%%%%%%%%%%%%%%%%%%%%%%%%%%%%%%%%%%%%%%%%%%%%%
% [X,Y,Z] = distnorm(x,y,z,xn,yn,zn,dist)
% x,y,z - arrays of coordinates of points on the original surface
% xn,yn,zn - arrays of coordinates of points normal to original surface
% dist - distance of new point along vector
%%%%%%%%%%%%%%%%%%%%%%%%%%%%%%%%%%%%%%%%%%%%%%%%%%%%%%%%%%%%%%%%%%%%%%%%%%%%%%%

%normalize  x,y,z
x_nrm = xn-x;
y_nrm = yn-y;
z_nrm = zn-z;

[THETA,PHI,R] = cart2sph(x_nrm,y_nrm,z_nrm);
R = R*0+dist;
```

```
[X,Y,Z] = sph2cart(THETA,PHI,R);

X = X+x;
Y = Y+y;
Z = Z+z;


function [X,Y,Z] = hemisphere(res,side)
%%%%%%%%%%%%%%%%%%%%%%%%%%%%%%%%%%%%%%%%%%%%%%%%%%%%%%%%%%%%%%%%%%%%%%%%%%%%%%%
% [X,Y,Z] = hemisphere(res,side)
% res - resultion of sphere
% side - 1 outputs upper half of sphere, 0 outputs lower half of sphere
%%%%%%%%%%%%%%%%%%%%%%%%%%%%%%%%%%%%%%%%%%%%%%%%%%%%%%%%%%%%%%%%%%%%%%%%%%%%%%%

[x,y,z] = sphere(res);
r = size(z,1);
row = ceil(r/2);
rup = (r-row+1):r;
rlo = 1:row;

if side == 1
    X = x(rup,1:end);
    Y = y(rup,1:end);
    Z = z(rup,1:end);
elseif side == 0
    X = x(rlo,1:end);
    Y = y(rlo,1:end);
    Z = z(rlo,1:end);
else
    Z = z;
end
```

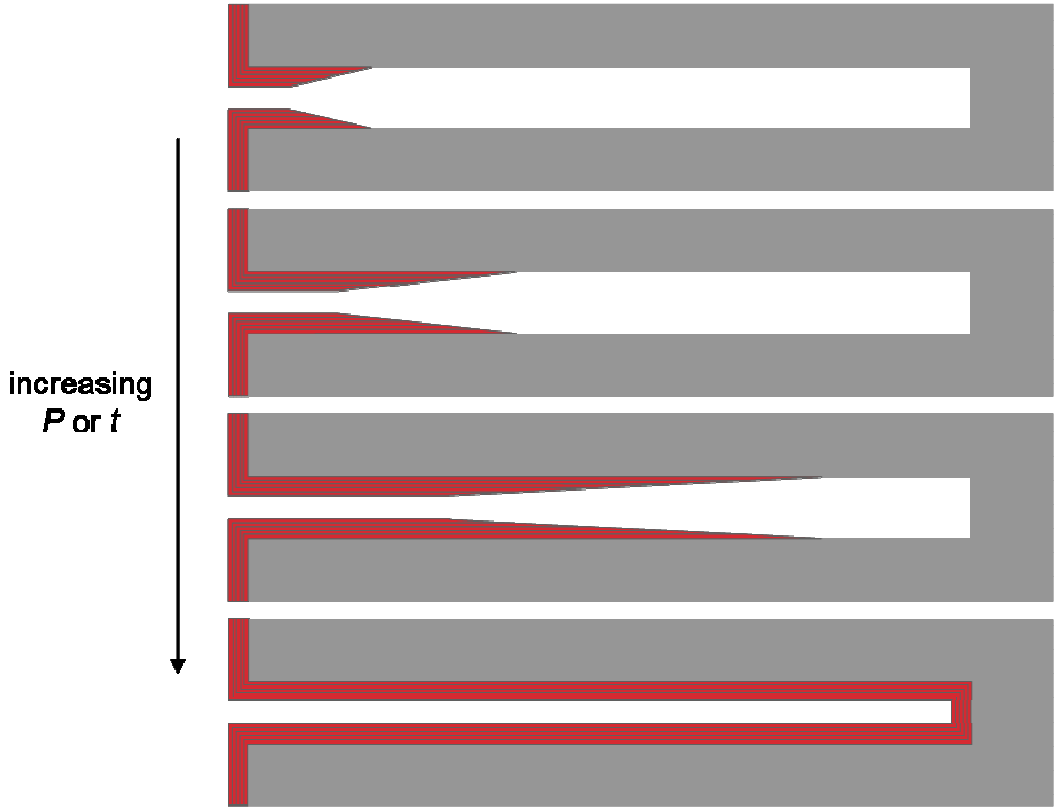

Figure A.3: As chamber pressure P and/or dose time t increase, depth at which films will deposit conformally increases; Slope of non-conformal region flattens.

References

[1] E. Robertson, P. Banerjee, I. Perez *et al.*, "Influence of underlying substrate topography on pattern formation of ALD films," 2009.

[2] W. Y. Leong, A. C. Churchill, D. J. Robbins *et al.*, "A self-aligned epitaxially grown channel MOSFET device architecture for strained Si/SiGe systems," *Thin Solid Films,* vol. 369, no. 1-2, pp. 375-378, Jul 3, 2000.

[3] G. W. Rubloff, "Maskless Selected Area Processing," *Journal of Vacuum Science & Technology B,* vol. 7, no. 6, pp. 1454-1461, Nov-Dec, 1989.

[4] S. L. Zhang, and U. Smith, "Self-aligned silicides for ohmic contacts in complementary metal-oxide-semiconductor technology: TiSi2, CoSi2 and NiSi," *Journal of Vacuum Science & Technology A,* vol. 22, no. 4, pp. 1361-1370, Jul-Aug, 2004.

[5] C. H. Liu, J. A. Zapien, Y. Yao *et al.*, "High-density, ordered ultraviolet light-emitting ZnO nanowire arrays," *Advanced Materials,* vol. 15, no. 10, pp. 838-+, May, 2003.

[6] K. Nielsch, R. B. Wehrspohn, J. Barthel *et al.*, "Hexagonally ordered 100 nm period nickel nanowire arrays," *Applied Physics Letters,* vol. 79, no. 9, pp. 1360-1362, Aug, 2001.

[7] M. J. Pellin, P. C. Stair, G. Xiong *et al.*, "Mesoporous catalytic membranes: Synthetic control of pore size and wall composition," *Catalysis Letters,* vol. 102, no. 3-4, pp. 127-130, Aug, 2005.

[8] C. R. Martin, "NANOMATERIALS - A MEMBRANE-BASED SYNTHETIC APPROACH," *Science,* vol. 266, no. 5193, pp. 1961-1966, Dec, 1994.

[9] H. Masuda, and K. Fukuda, "ORDERED METAL NANOHOLE ARRAYS MADE BY A 2-STEP REPLICATION OF HONEYCOMB STRUCTURES OF ANODIC ALUMINA," *Science,* vol. 268, no. 5216, pp. 1466-1468, Jun, 1995.

[10] A. B. F. Martinson, M. S. Goes, F. Fabregat-Santiago *et al.*, "Electron Transport in Dye-Sensitized Solar Cells Based on ZnO Nanotubes: Evidence for Highly Efficient Charge Collection and Exceptionally Rapid Dynamics," *Journal of Physical Chemistry A,* vol. 113, no. 16, pp. 4015-4021, Apr, 2009.

[11] I. Perez, E. Robertson, P. Banerjee *et al.*, "TEM-Based Metrology for HfO2 Layers and Nanotubes Formed in Anodic Aluminum Oxide Nanopore Structures," *Small,* vol. 4, no. 8, pp. 1223-1232, 2008.

[12] G. E. Thompson, and G. C. Wood, "Anodic Films on Aluminum," *Treatise on*

Materials Science and Technology, J. C. Scully, ed., pp. 205-329, New York, New York: Academic Press, 1983.

[13] H. Masuda, H. Yamada, M. Satoh *et al.*, "Highly ordered nanochannel-array architecture in anodic alumina," *Applied Physics Letters,* vol. 71, no. 19, pp. 2770-2772, Nov, 1997.

[14] K. Nielsch, J. Choi, K. Schwirn *et al.*, "Self-ordering regimes of porous alumina: The 10% porosity rule," *Nano Letters,* vol. 2, no. 7, pp. 677-680, Jul, 2002.

[15] H. Masuda, K. Nishio, and N. Baba, "FABRICATION OF A ONE-DIMENSIONAL MICROHOLE ARRAY BY ANODIC-OXIDATION OF ALUMINUM," *Applied Physics Letters,* vol. 63, no. 23, pp. 3155-3157, Dec, 1993.

[16] C. R. Martin, "Membrane-based synthesis of nanomaterials," *Chemistry of Materials,* vol. 8, no. 8, pp. 1739-1746, Aug, 1996.

[17] C. R. Martin, and P. Kohli, "The emerging field of nanotube biotechnology," *Nature Reviews Drug Discovery,* vol. 2, no. 1, pp. 29-37, Jan, 2003.

[18] S. J. Son, X. Bai, and S. B. Lee, "Inorganic hollow nanoparticles and nanotubes in nanomedicine. Part 1. Drug/gene delivery applications," *Drug Discovery Today,* vol. 12, no. 15-16, pp. 650-656, Aug, 2007.

[19] S. J. Son, X. Bai, A. Nan *et al.*, "Template synthesis of multifunctional nanotubes for controlled release." pp. 143-152.

[20] B. He, S. J. Son, and S. B. Lee, "Shape-coded silica nanotubes for biosensing," *Langmuir,* vol. 22, no. 20, pp. 8263-8265, Sep, 2006.

[21] N. I. Kovtyukhova, T. E. Mallouk, and T. S. Mayer, "Templated surface sol-gel synthesis of SiO2 nanotubes and SiO2-insulated metal nanowires," *Advanced Materials,* vol. 15, no. 10, pp. 780-+, May, 2003.

[22] N. L. Kovtyukhova, and T. E. Mallouk, "Nanowire p-n heterojunction diodes made by templated assembly of multilayer carbon-nanotube/polymer/semiconductor-particle shells around metal nanowires," *Advanced Materials,* vol. 17, no. 2, pp. 187-+, Jan, 2005.

[23] A. B. F. Martinson, J. W. Elam, J. T. Hupp *et al.*, "ZnO nanotube based dye-sensitized solar cells ZnO nanotube based dye-sensitized solar cells," *Nano Letters,* vol. 7, no. 8, pp. 2183-2187, Aug, 2007.

[24] A. B. F. Martinson, J. W. Elam, J. Liu *et al.*, "Radial electron collection in dye-sensitized solar cells," *Nano Letters,* vol. 8, no. 9, pp. 2862-2866, Sep, 2008.

[25] A. B. F. Martinson, T. W. Hamann, M. J. Pellin *et al.*, "New architectures for dye-senstized solar cells," *Chemistry-a European Journal,* vol. 14, no. 15, pp. 4458-4467, 2008.

[26] R. Liu, and S. B. Lee, "MnO2/Poly(3,4-ethylenedioxythiophene) coaxial nanowires by one-step coelectrodeposition for electrochemical energy storage," *Journal of the American Chemical Society,* vol. 130, no. 10, pp. 2942-2943, Mar, 2008.
[27] R. Xiao, S. Il Cho, R. Liu *et al.*, "Controlled electrochemical synthesis of conductive polymer nanotube structures," *Journal of the American Chemical Society,* vol. 129, no. 14, pp. 4483-4489, Apr, 2007.
[28] I. Ichinose, H. Senzu, and T. Kunitake, "A surface sol-gel process of TiO2 and other metal oxide films with molecular precision," *Chemistry of Materials,* vol. 9, no. 6, pp. 1296-&, Jun, 1997.
[29] D. Routkevitch, T. Bigioni, M. Moskovits *et al.*, "Electrochemical fabrication of CdS nanowire arrays in porous anodic aluminum oxide templates," *Journal of Physical Chemistry,* vol. 100, no. 33, pp. 14037-14047, Aug, 1996.
[30] W. Lee, R. Scholz, K. Niesch *et al.*, "A template-based electrochemical method for the synthesis of multisegmented metallic nanotubes," *Angewandte Chemie-International Edition,* vol. 44, no. 37, pp. 6050-6054, 2005.
[31] M. S. Sander, M. J. Cote, W. Gu *et al.*, "Template-assisted fabrication of dense, aligned arrays of titania nanotubes with well-controlled dimensions on substrates," *Advanced Materials,* vol. 16, no. 22, pp. 2052-+, Nov 18, 2004.
[32] K. B. Shelimov, D. N. Davydov, and M. Moskovits, "Template-grown high-density nanocapacitor arrays," *Applied Physics Letters,* vol. 77, no. 11, pp. 1722-1724, Sep 11, 2000.
[33] M. Leskela, and M. Ritala, "Atomic layer deposition chemistry: Recent developments and future challenges," *Angewandte Chemie-International Edition,* vol. 42, no. 45, pp. 5548-5554, 2003.
[34] B. Kang, and G. Ceder, "Battery materials for ultrafast charging and discharging," *Nature,* vol. 458, no. 7235, pp. 190-193, Mar, 2009.
[35] L. Young, *Anodic Oxide Films*, New York: Academic Press, 1961.
[36] R. C. Furneaux, G. E. Thompson, and G. C. Wood, "Application of Ultramicrotomy to Electron-Optical Examination of Surface-Films on Aluminum," *Corrosion Science,* vol. 18, no. 10, pp. 853-&, 1978.
[37] I. Vrublevsky, V. Parkoun, V. Sokol *et al.*, "Study of chemical dissolution of the barrier oxide layer of porous alumina films formed in oxalic acid using a re-anodizing technique," *Applied Surface Science,* vol. 236, no. 1-4, pp. 270-277, Sep, 2004.
[38] A. P. Li, F. Muller, A. Birner *et al.*, "Hexagonal pore arrays with a 50-420 nm interpore distance formed by self-organization in anodic alumina," *Journal of Applied Physics,* vol. 84, no. 11, pp. 6023-6026, Dec, 1998.

[39] Author ed.^eds., "Nanostructured Materials in Electrochemistry," Weinheim: WILEY-VCH Verlag GmbH & Co. KGaA, 2008, p.^pp. Pages.
[40] J. P. O'Sullivan, and G. C. Wood, "MORPHOLOGY AND MECHANISM OF FORMATION OF POROUS ANODIC FILMS ON ALUMINIUM," *Proceedings of the Royal Society of London Series a-Mathematical and Physical Sciences,* vol. 317, no. 1531, pp. 511-&, 1970.
[41] H. Masuda, and M. Satoh, "Fabrication of gold nanodot array using anodic porous alumina as an evaporation mask," *Japanese Journal of Applied Physics Part 2-Letters,* vol. 35, no. 1B, pp. L126-L129, Jan, 1996.
[42] K. Shimizu, K. Kobayashi, G. E. Thompson *et al.*, "DEVELOPMENT OF POROUS ANODIC FILMS ON ALUMINUM," *Philosophical Magazine a-Physics of Condensed Matter Structure Defects and Mechanical Properties,* vol. 66, no. 4, pp. 643-652, Oct, 1992.
[43] S. I. Cho, W. J. Kwon, S. J. Choi *et al.*, "Nanotube-based ultrafast electrochromic display," *Advanced Materials,* vol. 17, no. 2, pp. 171-+, Jan, 2005.
[44] J. W. Elam, D. Routkevitch, P. P. Mardilovich *et al.*, "Conformal coating on ultrahigh-aspect-ratio nanopores of anodic alumina by atomic layer deposition," *Chemistry of Materials,* vol. 15, no. 18, pp. 3507-3517, 2003.
[45] G. Xiong, J. W. Elam, H. Feng *et al.*, "Effect of atomic layer deposition coatings on the surface structure of anodic aluminum oxide membranes," *Journal of Physical Chemistry B,* vol. 109, no. 29, pp. 14059-14063, Jul, 2005.
[46] R. G. Gordon, D. Hausmann, E. Kim *et al.*, "A kinetic model for step coverage by atomic layer deposition in narrow holes or trenches," *Chemical Vapor Deposition,* vol. 9, no. 2, pp. 73-78, Mar, 2003.
[47] M. A. Cameron, I. P. Gartland, J. A. Smith *et al.*, "Atomic layer deposition of SiO2 and TiO2 in alumina tubular membranes: Pore reduction and effect of surface species on gas transport," *Langmuir,* vol. 16, no. 19, pp. 7435-7444, Sep, 2000.
[48] M. K. Gobbert, V. Prasad, and T. S. Cale, "Modeling and simulation of atomic layer deposition at the feature scale," *Journal of Vacuum Science & Technology B,* vol. 20, no. 3, pp. 1031-1043, May-Jun, 2002.
[49] J. Y. Kim, J. H. Ahn, S. W. Kang *et al.*, "Step coverage modeling of thin films in atomic layer deposition," *Journal of Applied Physics,* vol. 101, no. 7, Apr, 2007.
[50] A. Huczko, "Template-based synthesis of nanomaterials," *Applied Physics a-Materials Science & Processing,* vol. 70, no. 4, pp. 365-376, Apr, 2000.
[51] O. Jessensky, F. Muller, and U. Gosele, "Self-organized formation of hexagonal pore arrays in anodic alumina," *Applied Physics Letters,* vol. 72, no. 10, pp. 1173-1175,

Mar 9, 1998.
[52] F. Y. Li, L. Zhang, and R. M. Metzger, "On the growth of highly ordered pores in anodized aluminum oxide," *Chemistry of Materials,* vol. 10, no. 9, pp. 2470-2480, Sep, 1998.
[53] S. K. Gandhi, *VLSI Fabrication Principles: Silicon and gallium arsenide*, 2nd ed., p.^pp. 525, New York: John Wiley & Sons, 1994, Ch. 8.
[54] L. F. Hakim, J. Blackson, S. M. George *et al.*, "Nanocoating individual silica nanoparticles by atomic layer deposition in a fluidized bed reactor," *Chemical Vapor Deposition,* vol. 11, no. 10, pp. 420-425, Oct, 2005.
[55] L. F. Hakim, S. M. George, and A. W. Weimer, "Conformal nanocoating of zirconia nanoparticles by atomic layer deposition in a fluidized bed reactor," *Nanotechnology,* vol. 16, no. 7, pp. S375-S381, Jul, 2005.
[56] L. F. Hakim, J. A. McCormick, G. D. Zhan *et al.*, "Surface modification of titania nanoparticles using ultrathin ceramic films," *Journal of the American Ceramic Society,* vol. 89, no. 10, pp. 3070-3075, Oct, 2006.
[57] J. A. McCormick, B. L. Cloutier, A. W. Weimer *et al.*, "Rotary reactor for atomic layer deposition on large quantities of nanoparticles," *Journal of Vacuum Science & Technology A,* vol. 25, no. 1, pp. 67-74, Jan-Feb, 2007.
[58] D. B. Farmer, and R. G. Gordon, "Atomic layer deposition on suspended single-walled carbon nanotubes via gas-phase noncovalent functionalization," *Nano Letters,* vol. 6, no. 4, pp. 699-703, Apr, 2006.
[59] A. Javey, J. Guo, D. B. Farmer *et al.*, "Self-aligned ballistic molecular transistors and electrically parallel nanotube arrays," *Nano Letters,* vol. 4, no. 7, pp. 1319-1322, Jul, 2004.
[60] A. Javey, R. Tu, D. B. Farmer *et al.*, "High performance n-type carbon nanotube field-effect transistors with chemically doped contacts," *Nano Letters,* vol. 5, no. 2, pp. 345-348, Feb, 2005.
[61] R. Chen, and S. F. Bent, "Highly stable monolayer resists for atomic layer deposition on germanium and silicon," *Chemistry of Materials,* vol. 18, no. 16, pp. 3733-3741, Aug, 2006.
[62] P. de Rouffignac, and R. G. Gordon, "Atomic layer deposition of praseodymium aluminum oxide for electrical applications," *Chemical Vapor Deposition,* vol. 12, no. 2-3, pp. 152-157, Mar, 2006.
[63] P. de Rouffignac, J. S. Park, and R. G. Gordon, "Atomic layer deposition of Y2O3 thin films from yttrium tris(N,N'-diisopropylacetamidinate) and water," *Chemistry of Materials,* vol. 17, no. 19, pp. 4808-4814, Sep, 2005.

[64] P. de Rouffignac, A. P. Yousef, K. H. Kim *et al.*, "ALD of scandium oxide from scandium Tris(N,N-'-diisopropylacetamidinate) and water," *Electrochemical and Solid State Letters,* vol. 9, no. 6, pp. F45-F48, 2006.
[65] K. H. Kim, R. G. Gordon, A. Ritenour *et al.*, "Atomic layer deposition of insulating nitride interfacial layers for germanium metal oxide semiconductor field effect transistors with high-kappa oxide/tungsten nitride gate stacks," *Applied Physics Letters,* vol. 90, no. 21, May, 2007.
[66] Z. W. Li, and R. G. Gordon, "Thin, continuous, and conformal copper films by reduction of atomic layer deposited copper nitride," *Chemical Vapor Deposition,* vol. 12, no. 7, pp. 435-441, Jul, 2006.
[67] X. Y. Liu, S. Ramanathan, A. Longdergan *et al.*, "ALD of hafnium oxide thin films from tetrakis(ethylmethylamino)hafnium and ozone (vol 152, pg G213, 2005)," *Journal of the Electrochemical Society,* vol. 152, no. 5, pp. L9-L9, 2005.
[68] *Metrology*, 2005.
[69] K. Raidongia, D. Jagadeesan, M. Upadhyay-Kahaly *et al.*, "Synthesis, structure and properties of homogeneous BC4N nanotubes," *Journal Of Materials Chemistry,* vol. 18, no. 1, pp. 83-90, 2008.
[70] H. J. Shin, D. K. Jeong, J. G. Lee *et al.*, "Formation of TiO2 and ZrO2 nanotubes using atomic layer deposition with ultraprecise control of the wall thickness," *Advanced Materials,* vol. 16, no. 14, pp. 1197-+, Jul 19, 2004.
[71] P. Banerjee, I. Perez, L. Henn-Lecordier *et al.*, "Nanotubular metal-insulator-metal capacitor arrays for energy storage," *Nature Nanotechnology,* vol. 4, no. 5, pp. 292-296, May, 2009.
[72] A. Burke, "Ultracapacitors: why, how, and where is the technology," *Journal of Power Sources,* vol. 91, no. 1, pp. 37-50, Nov, 2000.
[73] B. E. Conway. "Electrochemistry Encyclopedia: Electrochemical Capacitors: Their Nature, Function, and Applications," http://electrochem.cwru.edu/ed/encycl/.
[74] F. Roozeboom, R. Elfrink, J. Verhoeven *et al.*, "High-value MOS capacitor arrays in ultradeep trenches in silicon," *Microelectronic Engineering,* vol. 53, no. 1-4, pp. 581-584, Jun, 2000.
[75] M. Kemell, M. Ritala, M. Leskela *et al.*, "Si/Al2O3/ZnO : Al capacitor arrays formed in electrochemically etched porous Si by atomic layer deposition." pp. 313-318.
[76] Q. F. Xing, G. Sasaki, and H. Fukunaga, "Interfacial microstructure of anodic-bonded Al/glass," *Journal of Materials Science-Materials in Electronics,* vol. 13, no. 2, pp. 83-88, Feb, 2002.

[77] H. K. Kim, J. Y. Kim, J. Y. Park *et al.*, "Metalorganic atomic layer deposition of TiN thin films using TDMAT and NH3," *Journal of the Korean Physical Society,* vol. 41, no. 5, pp. 739-744, 2002.
[78] L. Henn-Lecordier, W. Lei, M. Anderle *et al.*, "Real-time sensing and metrology for atomic layer deposition processes and manufacturing," *Journal of Vacuum Science & Technology B,* vol. 25, no. 1, pp. 130-139, 2007.
[79] J. C. Hackley, J. D. Demaree, and T. Gougousi, "Growth and interface of HfO2 films on H-terminated Si from a TDMAH and H2O atomic layer deposition process," *Journal of Vacuum Science & Technology A,* vol. 26, no. 5, pp. 1235-1240, Sep, 2008.
[80] P. Banerjee, and A. Ditali, "Uniqueness in activation energy and charge-to-breakdown of highly asymmetrical DRAM Al2O3 cell capacitors," *Ieee Electron Device Letters,* vol. 25, no. 8, pp. 574-576, Aug, 2004.
[81] J. H. Klootwijk, K. B. Jinesh, W. Dekkers *et al.*, "Ultrahigh capacitance density for multiple ALD-grown MIM capacitor stacks in 3-D silicon," *Ieee Electron Device Letters,* vol. 29, no. 7, pp. 740-742, Jul, 2008.
[82] R. L. Puurunen, and W. Vandervorst, "Island growth as a growth mode in atomic layer deposition: A phenomenological model," *Journal of Applied Physics,* vol. 96, no. 12, pp. 7686-7695, 2004.
[83] R. L. Puurunen, "Growth per cycle in atomic layer deposition: Real application examples of a theoretical model," *Chemical Vapor Deposition,* vol. 9, no. 6, pp. 327-332, 2003.
[84] R. L. Puurunen, "Analysis of hydroxyl group controlled atomic layer deposition of hafnium dioxide from hafnium tetrachloride and water," *Journal of Applied Physics,* vol. 95, no. 9, pp. 4777-4786, 2004.
[85] V. Dwivedi, and R. Adomaitis, "Multiscale simulation of atomic layer deposition in a nanoporous material," *ISR technical report, University of Maryland, College Park,* vol. *2008-21*, 2008.
[86] M. Rose, and J. W. Bartha, "Method to determine the sticking coefficient of precursor molecules in atomic layer deposition," *Applied Surface Science,* vol. 255, no. 13-14, pp. 6620-6623, Apr, 2009.
[87] D. R. Wolters, and J. J. Van Der Schoot, "DIelectric Breakdown in MOS devices, Part I: Defect-related and intrinsic breakdown " *Phillips Journal of Research,* vol. 40, no. 3, pp. 115-136, 1985.
[88] D. R. Wolters, and J. J. Van Der Schoot, "DIelectric Breakdown in MOS devices, Part II: Conditions for the intrinsic breakdown " *Phillips Journal of Research,* vol. 40, no. 3, pp. 137-163, 1985.